Computers and Fluids 306 (2026) 106947

Contents lists available at ScienceDirect

Computers and Fluids

journal homepage: www.elsevier.com/locate/compfluid

Non-orthogonal plane-marching parabolized stability equations for the secondary instability of crossflow vortices

Koen J. Groot [a,*], Jordi Casacuberta [b], Stefan Hickel [b]

[a] University of Wyoming, 1000 E. University, Laramie, 82071, WY, USA
[b] Delft University of Technology, Kluyverweg 1, Delft, 2629 HS, The Netherlands

ARTICLE INFO

Keywords:
Plane-marching parabolized stability equations (PSE)
Secondary crossflow instability
Laminar-turbulent transition

ABSTRACT

A detailed derivation, analysis, and verification is given for the non-orthogonal, plane-marching Parabolized Stability Equations (PSE) approach. In applying the approach to a flow distorted by a medium-amplitude crossflow vortex, we determine its linear secondary instability mechanisms. We show that converged solutions can be achieved for a broad frequency range with an existing stabilization method for the line-marching PSE approach. We verify that 1) solutions converge versus grid size in all dimensions, 2) primary disturbance solutions agree with line-marching PSE results, and 3) secondary disturbance solutions match amplitude and growth-rate evolution of reference Direct Numerical Simulation (DNS) results. We show how and why the *type*-II instability displays a delayed neutral point when modeled with the plane-marching approach versus the considered local stability approaches, whether the streamwise evolution of the distorted base flow is accounted for or not. This may explain why the *type*-II disturbance is scarcely captured by DNS in the literature.

1. Introduction

To predict and ultimately avoid crossflow-dominated boundary layers' transition to turbulence, it is necessary to have a detailed understanding of the secondary instability mechanisms [1]. This led to the development of secondary linear stability theory for the rotating-disk [2] and swept-wing scenario [3–5]. This theory revealed 3 main, unsteady instability mechanisms. Following the nomenclature of Malik et al. [4], there are two proper secondary instability mechanisms (called the z- and y-modes based on the shear layer they feed their energy from) and an instance of the traveling primary crossflow instability, subject to the distorted base flow. Koch et al. [5] called these same modes the *type*-I, -II, and -III modes, respectively. The *type*-I and -II modes are typically observed to be most amplified at frequencies that are an order of magnitude higher than *type*-III. Although the present article will continue to focus on crossflow-dominated boundary layers, the approach presented in this article could also help in many other scenarios, such as for the Rayleigh-Taylor and Richtmyer-Meskov instabilities [6–8].

Wassermann and Kloker [9] established a Direct Numerical Simulation (DNS) of the secondary-crossflow-instability problem to create a reference to quantify modeling error. Their domain is aligned with the leading-edge-orthogonal and -parallel ($x_\perp, z_{||}$) coordinates and shown in Fig. 1(a). Stability methods leverage simplifying assumptions, involving the slow variation of the flow along the crossflow vortices, to significantly reduce the computational cost [2–5]. To minimize the errors associated with these assumptions, the spanwise axis of the domain is placed parallel to the wave vector of the crossflow vortex (z_v), or, equivalently, orthogonal to its vortical axis (x_v) [3]. These directions are indicated in Fig. 1(b). Bonfigli and Kloker [10] set out to verify the results from these stability methods against the DNS, using both domain orientations corresponding to Fig. 1(a) and (b). One of Bonfigli & Kloker's main findings is that, to match growth rates, the DNS domain must match the alignment of the domain used for the secondary instability theory. To establish the match, Bonfigli & Kloker adapted Wasserman & Kloker's leading-edge-aligned domain (Fig. 1(a)) to instead be aligned with the local direction of the crossflow vortex (Fig. 1(b)). This allowed making the verification between the DNS and theory, because both make the same modeling assumptions. Although matching growth rates were established this way (see their Fig. 15), a small, inherent drawback was committed in making this arrangement: the distorted base flow is not exactly periodic in the direction orthogonal to the crossflow vortex. Li and Choudhari [11] provided the solution to this issue by using a non-orthogonal coordinate system. They placed their spanwise coordinate parallel to the leading edge (z), i.e. the formal periodic direction, and pointed their streamwise coordinate parallel to the axis of the crossflow vortex (x), see Fig. 1(c). An example of a favorable comparison of the

* Corresponding author.
E-mail address: kgroot@uwyo.edu (K.J. Groot).

https://doi.org/10.1016/j.compfluid.2025.106947
Received 15 July 2025; Received in revised form 25 November 2025; Accepted 14 December 2025
Available online 17 December 2025

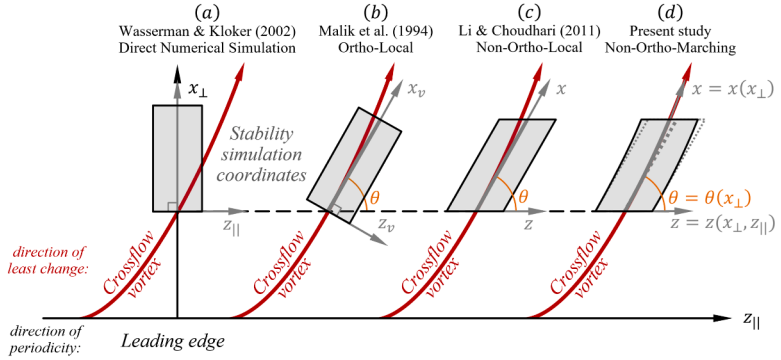

Fig. 1. Various numerical formulations of the secondary crossflow instability problem: leveraging the spanwise periodicity in $z_{||}$ and slow evolution along the crossflow vortex x_v to different extents.

most-amplified frequencies determined with a similar non-orthogonal instability approach against experimental data is given by Groot and Eppink [12].

With the advent of the plane-marching Parabolized Stability Equations (PSE) approach, popularly known as PSE-3D [13,14], formulated in a non-orthogonal and also nonlinear forms, instability methods are approaching the highest possible fidelity. The 'local' stability approaches, that are conceptually depicted in panels (*b*) and (*c*) of Fig. 1, neglect the slow streamwise evolution of the flow. That is, the base flow is modeled as invariant in the x_v-direction. This is commonly referred to as the parallel-flow assumption, even if the wall-normal velocity component of the distorted base flow should not be dropped from these methods, see Section 2.4 for the technical details. Upon using this assumption in local stability approaches, the crossflow vortex appears straight in the $x_\perp z_{||}$-plane to the secondary instability mechanisms, shown as the thick gray line in Fig. 1. In reality, however, crossflow vortices gradually curve in the $x_\perp z_{||}$-plane. Plane-marching approaches alleviate this model error of the local approaches by accounting for all effects attributed to slow streamwise evolution, see Fig. 1(*d*). Recently, Ambrosino et al. [15] verified secondary stability results when comparing solutions to the non-orthogonal plane-marching approach to a DNS of the *type*-I and -III mechanisms.

The present study provides a detailed derivation and analysis of the non-orthogonal, plane-marching approach for the computation of linear, secondary instability of crossflow vortices extending the work of Ambrosino et al. [15]. We evaluate local, quasi-local, and plane-marching approaches to the DNS case of Casacuberta et al. [16], which is characterized by a higher crossflow-vortex amplitude. To be specific, we extend the work of Ambrosino et al. [15] by demonstrating that:

1. the non-orthogonal, plane-marching approach is numerically consistent with a grid convergence study (which is rarely recorded in the literature);
2. the stabilization approach proposed by Andersson et al. [17] enables effectively achieving plane-marching results if residual ellipticity of the system would otherwise cause divergence, enabling producing results for a broad range of frequencies;
3. the approach matches against (orthogonal, line-marching) PSE results;
4. the marching aspect is necessary to produce accurate agreement with DNS for a higher-amplitude crossflow vortex for a particular instance of the *type*-III instability mechanism; and
5. the neutral point corresponding to the *type*-II instability mechanism is delayed when modeled with the plane-marching approach, which may explain why previous attempts at DNS of that mechanism are scarce in the literature.

The remainder of this article is structured as follows. First, the DNS of the primary and secondary instabilities will be discussed in Section 2.1. Second, the non-orthogonal, plane-marching approach is described in detail in Sections 2.2–2.7. An overview of the results is given in Section 3.1, grid convergence and verification against (line-marching) PSE is demonstrated in Section 3.2, verification against DNS in Section 3.3, and the delayed neutral point of the *type*-II instability is elaborated in Section 3.4. The article is concluded in Section 4.

2. Methodology

To introduce nomenclature indicating the various ways in which the flow field will be decomposed, we will first express our variables in a leading-edge-orthogonal coordinate system, where $x_\perp$ is orthogonal to the leading edge, y is wall-normal, and $z_{||}$ is parallel to the leading edge. We consider a negative sweep angle, to most closely reflect the experiments by Rius-Vidales and Kotsonis [18,19,20], which implies that the positive $z_{||}$-direction, in a right-handed coordinate system, points toward the root of the (backward-)swept wing. An instantaneous flow variable, q, will be decomposed as:

$$q(x_\perp, y, z_{||}, t) = \underbrace{\overline{Q}(x_\perp, y) + \mathring{q}(x_\perp, y, z_{||})}_{\mathring{\overline{Q}}(x_\perp, y, z_{||})} + q'(x_\perp, y, z_{||}, t), \tag{1}$$

where $\overline{Q} = \overline{Q}(x_\perp, y)$ denotes the undisturbed, laminar base flow, $\mathring{q} = \mathring{q}(x_\perp, y, z_{||})$ is the primary crossflow disturbance to the undisturbed base flow, $\mathring{\overline{Q}} = \overline{Q} + \mathring{q}$ is the distorted base flow, and $q' = q'(x_\perp, y, z_{||}, t)$ the unsteady disturbance to the distorted base flow, $\mathring{\overline{Q}}$. In what follows, $\mathring{q}$ will be assumed to consist of stationary crossflow vortices. For that reason, the time dependence of $\mathring{q}$ and $\mathring{\overline{Q}}$ is dropped in Eq. (1). If, instead, the travelling crossflow instability causes the primary disturbance, $\mathring{q}$ and $\mathring{\overline{Q}}$ would depend on time.

2.1. Direct numerical simulation

In this subsection, we give a brief overview of the set-up of the Direct Numerical Simulation (DNS) that is elaborated on in more detail by Casacuberta et al. [16,21,22]. We consider the flow over a swept flat plate that models the 45°-swept wing considered by Rius-Vidales and Kotsonis [19]. The sides of the DNS domain are aligned with the leading-edge-orthogonal $x_\perp$-, wall-normal y-, and leading-edge-parallel $z_{||}$-directions.

The inlet of the domain is virtually placed at 5 % of the chord downstream of the leading edge of the wing considered by Rius-Vidales and Kotsonis [19]; a Falkner–Skan–Cooke profile is there imposed as the inflow condition. From there onward, the free-stream velocity distribution is matched against the pressure distribution as measured by Rius-Vidales and Kotsonis [19]. Hence, from the inlet onward, the boundary-layer evolution is non-self-similar. The boundary-layer thickness at the inlet

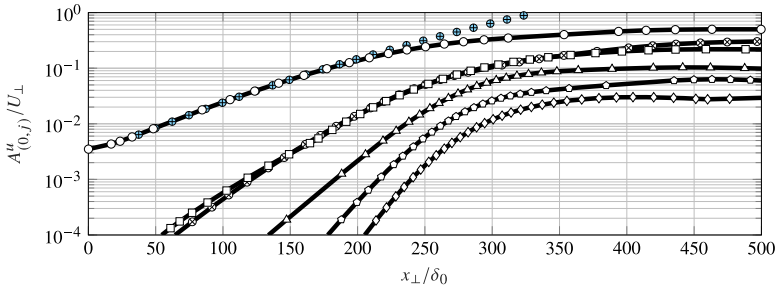

Fig. 2. Streamwise evolution of the primary, stationary crossflow disturbance amplitude from the DNS (lines with white symbols) and linear PSE (blue symbols). From top to bottom, the circles represent: $A^u_{(0,1)}$; crossed circles: $A^u_{(0,0)}$; squares: $A^u_{(0,2)}$; triangles: $A^u_{(0,3)}$; pentagons: $A^u_{(0,4)}$; and diamonds: $A^u_{(0,5)}$.

(based on 99 % of the leading-edge-orthogonal velocity component), denoted by δ_0, equals 0.771 mm. Together with the free-stream velocity in the direction orthogonal to the leading edge at the inflow: $U_\perp = 15.1$ m/s and the kinematic viscosity, δ_0 yields a local Reynolds number of 791.365. Also matching Rius-Vidales and Kotsonis [19], the sweep angle is incorporated by specifying the leading-edge-parallel free-stream velocity $W_{||}$ equal to $-1.24U_\perp$.

In the direction parallel to the leading edge, the DNS domain models one crossflow-vortex wavelength, $\lambda_{z_{||}} = 7.5$ mm in the $z_{||}$-direction, representative of the most-amplified disturbance in the case considered by Rius-Vidales and Kotsonis [19]. A stationary crossflow disturbance is triggered at the inlet of the domain by imposing a crossflow instability mode as obtained from Linear Stability Theory (LST) while assigning it a finite amplitude. Following their definition, the amplitude $A^u_{(0,1)}$ represents the maximum in the wall-normal direction of twice the fundamental Fourier mode of the stationary perturbation field as transformed in the direction parallel to the leading edge. The vortices observed in the Particle Image Velocimetry (PIV) measurements by Rius-Vidales and Kotsonis [19] were iteratively determined to have: $A^u_{(0,1)}/U_\perp = 2.6\times10^{-2}$. In this study, we consider the smaller amplitude $A^u_{(0,1)}/U_\perp = 3.5\times10^{-3}$. This is advantageous for our verification purposes: to create a relatively long streamwise extent in the DNS over which the secondary instability mechanisms display linear dynamics. To put this initial amplitude in context, the streamwise evolution is shown in Fig. 2.

The DNS are performed with a conservative finite-volume flow solver [23–25]. The computational grid is highly refined, with 6760, 576, and 72 points along the $x_\perp$-, y-, and $z_{||}$-directions, respectively. This yields more than 70 grid points to cover the wall-normal extent of the boundary layer at the inflow. For the unperturbed base-flow solution, the minimum grid spacing is $\Delta x^+_\perp = 5.68$, $\Delta y^+ = 0.52$, and $\Delta z^+_{||} = 4.73$ in wall units.

To compute the steady flow, the Selective Frequency Damping (SFD) approach is used [26,27]. To compute the unsteady flow field, wall blowing and suction is applied at selected frequencies of interest and the $x_\perp$-range denoted by: $x_{\perp,\text{start}} < x_\perp < x_{\perp,\text{end}}$. That is, the wall-normal velocity is modulated continuously in time according to the expression:

$$v(x_\perp, 0, z_{||}, t) = A_0\, g(x_\perp)\cos\{2\pi(z_{||}/\lambda_0 + f_0 t)\}, \tag{2}$$

where t is time and A_0, $\lambda_0 = 7.5\,\text{mm} = 9.728\delta_0$, f_0, and g are the forcing amplitude, wavelength in the $z_{||}$-direction, cyclic frequency, and streamwise distribution of the wall disturbance, respectively. For the function g, we use a smooth, streamwise distribution:

$$g(x_\perp) = \left(4\frac{(x_\perp - x_{\perp,\text{start}})(x_{\perp,\text{end}} - x_\perp)}{(x_{\perp,\text{end}} - x_{\perp,\text{start}})^2}\right)^3, \tag{3}$$

which vanishes in its value and its first and second derivatives at the start- and end-points of the forcing strip: $x_\perp = x_{\perp,\text{start}}$ and $x_{\perp,\text{end}}$.

For the verification purposes of this article, we focus on two frequencies, $f_0 = 6$ kHz and 1 kHz, that are forced independently. *A-priori* stability analyses, with the approaches described in Section 2.4, showed that 6 kHz is close to the most-amplified instance of the *type*-I mechanism. The *type*-III mechanism happens to display interesting dynamics at frequencies around at 1 kHz, that are relevant for our purposes of verification. The function $g = g(x_\perp)$ is started $24\delta_0$ upstream of the neutral point for each frequency, as computed with the stability approaches, which represents about two streamwise wavelengths of the stationary crossflow vortex. In particular, $x_{\perp,\text{start}}/\delta_0 = 251$ and 201 for $f_0 = 6$ kHz and 1 kHz, respectively, and $x_{\perp,\text{end}} - x_{\perp,\text{start}} = 12\delta_0$ for both frequencies. The wall-disturbance amplitude A_0 is set equal to $A_0/U_\perp = 10^{-3}$ for $f_0 = 6$ kHz and $A_0/U_\perp = 10^{-5}$ for 1 kHz. Preliminary tests demonstrated that these wall-disturbance amplitudes yield a significantly long $x_\perp$-range over which the unsteady disturbances showed exponential growth.

2.2. Non-orthogonal coordinate transformation

The distorted base flow (and hence the perturbation problem) is periodic in the direction parallel to the leading edge, $z_{||}$, while the variation of the distorted base flow is the least in the direction of the vortical axis of the crossflow vortices, x_v in Fig. 1(*b*). Although this will be quantified in Fig. 5; qualitatively, the 'spanwise phase' of the vortex shape is constant in the x_v-direction, while the phase changes along the $x_\perp$-direction. In swept-wing boundary layers, it is very unusual for the x_v- and $z_{||}$-directions to make a right angle. The crossflow vortices' axis is usually just a few degrees removed from the local inviscid streamline [28], and the inviscid streamline, in turn, makes an angle of about the overall sweep angle versus the leading-edge-orthogonal $x_\perp$-direction far enough downstream of the leading edge.

To minimize the model error associated to the parallel-flow or slow-stream-wise-evolution assumption, therefore, the stability problem for q' should be re-expressed in a non-orthogonal coordinate system. This approach was originally proposed by Li and Choudhari [11] for the stability problem that neglects all streamwise evolution of the shape of the disturbance in the $z_{||}y$-plane (which will be denoted by $\tilde{q}$ in Eq. (12) later in the article and is traditionally called the disturbance shape function), which will here be referred to as the 'local' problem. Despite the treatment of Li and Choudhari [11], incorporating a non-orthogonal coordinate system is uncommon in the literature. A comprehensive derivation enables properly revealing the generalization established by the non-orthogonal, plane-marching approach, which accounts for the slow streamwise evolution of the disturbance's shape in the $z_{||}y$-plane. Hence, we here elaborate on the formulation of the equations governing the secondary instability in detail.

The relation between the orthogonal $(x_\perp, z_{||})$ and non-orthogonal (x,z) coordinates is illustrated in Fig. 3. The angle θ is defined between the leading-edge-orthogonal $x_\perp$-direction and the vortical x-axis of the crossflow vortices; in Section 2.3, it will be shown that the latter direction can be unambiguously defined. In considering a long streamwise domain length, the crossflow vortices undergo a significant development. Therefore, θ varies in the streamwise direction: $\theta = \theta(x_\perp)$. In assuming that the crossflow vortices are periodic in the leading-edge-parallel $z_{||}$-direction and modeling a single wavelength in the laminar base flow,

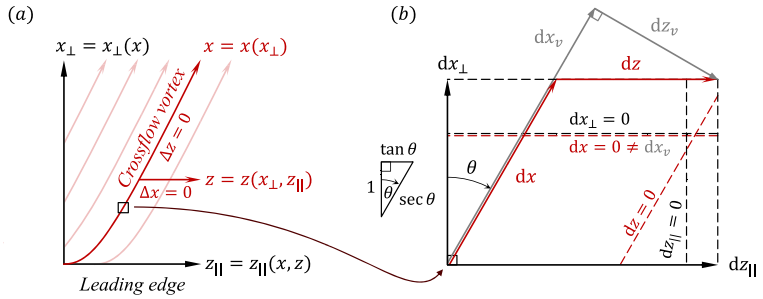

Fig. 3. Finite (*a*) and infinitesimal (*b*) orthogonal ($x_\perp$,$z_{||}$) and non-orthogonal (x,z) coordinate systems. The crossflow vortices' periodicity renders $\theta = \theta(x_\perp)$ and $x = x(x_\perp)$. Shown crossflow vortices' orientation corresponds to a positive sweep angle (positive $z_{(||)}$-direction points to wing tip).

θ is not a function of $z_{||}$. Furthermore, note that the non-orthogonal z-coordinate is parallel to $z_{||}$ and it differs from $z_{||}$ by a translation. The orientation of the parameters in Fig. 3 corresponds to a positive sweep angle ($z_{||}$ pointing toward the wing-tip on a backward-swept wing). Due to the use of a negative sweep angle ($z_{||}$ then points toward the root of the wing), θ will be negative in the present study.

In considering infinitesimal distances in Fig. 3(*b*), Eq. (4)(a – d) relate the orthogonal ($x_\perp z_{||}$) and non-orthogonal (xz) coordinates:

$$\mathrm{d}x = \mathrm{d}x_\perp / \cos\theta = \mathrm{d}x_\perp \sec\theta, \tag{4a}$$

$$\mathrm{d}z = \mathrm{d}z_{||} - \mathrm{d}x_\perp \tan\theta; \tag{4b}$$

$$\mathrm{d}x_\perp = \mathrm{d}x \cos\theta, \tag{4c}$$

$$\mathrm{d}z_{||} = \mathrm{d}z + \mathrm{d}x \sin\theta. \tag{4d}$$

To obtain the finite coordinate relations (i.e. for x, z, $x_\perp$, $z_{||}$, etc., not their differentials), Eqs. (4) need to be integrated from a reference point onward, while accounting for $\theta = \theta(x_\perp)$. When graphing the shape of the disturbance, we can invoke the spanwise periodicity of the flowfield to arbitrarily translate the solution in the spanwise direction to keep the same portion of the vortex in view.

The governing equations for q' in Cartesian coordinates are commonly available in the literature, see [29]. To reexpress these equations in the xz-coordinates, we first realize that we are expressing the same function in a different basis, i.e. different coordinates: $f_\perp = f_\perp(x_\perp, z_{||}) = f(x, z) = f$. The transformation then proceeds by invoking the chain rule on $f = f(x, z) = f\{x(x_\perp), z(x_\perp, z_{||})\}$ and using Eqs. (4). The derivatives with respect to the $x_\perp$- and $z_{||}$-coordinates transform as follows:

$$\left.\frac{\partial f_\perp}{\partial x_\perp}\right|_{z_{||}} = \left.\frac{\partial f}{\partial x}\right|_z \sec\theta - \left.\frac{\partial f}{\partial z}\right|_x \tan\theta; \tag{5a}$$

$$\left.\frac{\partial f_\perp}{\partial z_{||}}\right|_{x_\perp} = \left.\frac{\partial f}{\partial z}\right|_x \tag{5b}$$

The non-trivial inverse of Eq. (5a) is written:

$$\left.\frac{\partial f}{\partial x}\right|_z = \left.\frac{\partial f_\perp}{\partial x_\perp}\right|_{z_{||}} \cos\theta + \left.\frac{\partial f_\perp}{\partial z_{||}}\right|_{x_\perp} \sin\theta. \tag{6}$$

This relationship is useful for obtaining the derivatives of the distorted base-flow quantities in the x- and z-directions. To derive the equations with computer algebra software, it is useful to define the metric tensors. The forward and inverse transformation rules lead to the following, respectively covariant and contravariant, non-diagonal metric tensors [30, Section 7.23]:

$$g_{ij} = \frac{\partial y^k}{\partial x^i}\frac{\partial y^k}{\partial x^j} \underset{\text{as a matrix}}{\overset{\text{expressing}}{=}} \begin{bmatrix} 1 & 0 & \sin\theta \\ 0 & 1 & 0 \\ \sin\theta & 0 & 1 \end{bmatrix}; \tag{7a}$$

$$g^{ij} = \frac{\partial x^i}{\partial y^k}\frac{\partial x^j}{\partial y^k} \underset{\text{as a matrix}}{\overset{\text{expressing}}{=}} \begin{bmatrix} \sec^2\theta & 0 & -\sec\theta\tan\theta \\ 0 & 1 & 0 \\ -\sec\theta\tan\theta & 0 & \sec^2\theta \end{bmatrix}, \tag{7b}$$

where summation over the index k is implied and x^i and y^i represent the nonorthogonal ($x^1 = x$, $x^2 = y$, $x^3 = z$) and Cartesian coordinates ($y^1 = x_\perp$, $y^2 = y = x^2$, $y^3 = z_{||}$), respectively.

To transform the Laplacian, second derivatives are needed. In developing these derivatives from Eqs. (4), it is important to account for the dependence of θ on $x_\perp$. The cross-derivative is also provided for completeness:

$$\frac{\partial^2 f_\perp}{\partial x_\perp^2} = \left(\frac{\partial^2 f}{\partial x^2} - \frac{\partial f}{\partial z}\frac{\mathrm{d}\theta}{\mathrm{d}x_\perp}\right)\sec^2\theta + \left(\frac{\partial f}{\partial x}\frac{\mathrm{d}\theta}{\mathrm{d}x_\perp} - 2\frac{\partial^2 f}{\partial x\,\partial z}\right)\sec\theta\tan\theta + \frac{\partial^2 f}{\partial z^2}\tan^2\theta; \tag{8a}$$

$$\frac{\partial^2 f_\perp}{\partial x_\perp \partial z_{||}} = \frac{\partial^2 f}{\partial x\,\partial z}\sec\theta - \frac{\partial^2 f}{\partial z^2}\tan\theta; \tag{8b}$$

$$\frac{\partial^2 f_\perp}{\partial z_{||}^2} = \frac{\partial^2 f}{\partial z^2}. \tag{8c}$$

Upon forming the Laplacian, the coefficients of $\partial^2/\partial z^2$ combine into $\sec^2\theta$.

From here onward, the subscript $\perp$ will be given a different purpose. Instead of indicating the functional dependency on the $x_\perp z_{||}$-coordinates, it will indicate the velocity component in the leading-edge-orthogonal $x_\perp$-direction. To clearly disambiguate the subscript convention from here onward, the components of the ordered sets $(\mathring{\overline{U}}_\perp, \mathring{\overline{V}}, \mathring{\overline{W}}_{||})$ and $(u'_\perp, v', w'_{||})$ respectively correspond to the distorted base-flow and perturbation velocity components in the orthogonal $x_\perp$-, y-, and $z_{||}$-directions. The same convention will be used for the shape functions $(\tilde{u}_\perp, \tilde{v}, \tilde{w}_{||})$, that will be defined in Section 2.4. The velocity components in the non-orthogonal directions are obtained from Eqs. (4a) and (4b):

$$\mathring{\overline{U}} = \mathring{\overline{U}}_\perp \sec\theta; \qquad \mathring{\overline{W}} = \mathring{\overline{W}}_{||} - \mathring{\overline{U}}_\perp \tan\theta. \tag{9}$$

The same transformation can be used to obtain (u', w') and $(\tilde{u}, \tilde{w})$.

2.3. Definition of the angle θ

The intended parabolized nature of the stability approach dictates that, in order for the non-orthogonal coordinate formulation to be effective, the flow must possess a well-defined direction in which it varies least. For the present crossflow-vortex case, this direction exists. To demonstrate this, we determine the θ-value that minimizes the x-derivative of $\mathring{\overline{U}}_\perp$, $\mathring{\overline{V}}$, $\mathring{\overline{W}}_{||}$, or their root-mean-square combination. We assessed both the maximum value and the root-mean-square value as evaluated over the entire $z_{(||)}y$-plane at a given $x_\perp$-station. Fig. 4 shows that, as the crossflow vortex reaches a sufficient amplitude and saturates, all these candidate θ-values collapse onto a common direction that is about 5° closer to the $x_\perp$-direction than the inviscid streamline is, which is what is expected of the crossflow-vortex core.

From here onward, we use the angle $\theta = \theta_{\min}$ that minimizes the root-mean-square of the x-derivatives of $\mathring{\overline{U}}_\perp$, $\mathring{\overline{V}}$, and $\mathring{\overline{W}}_{||}$ in the zy-plane, i.e.

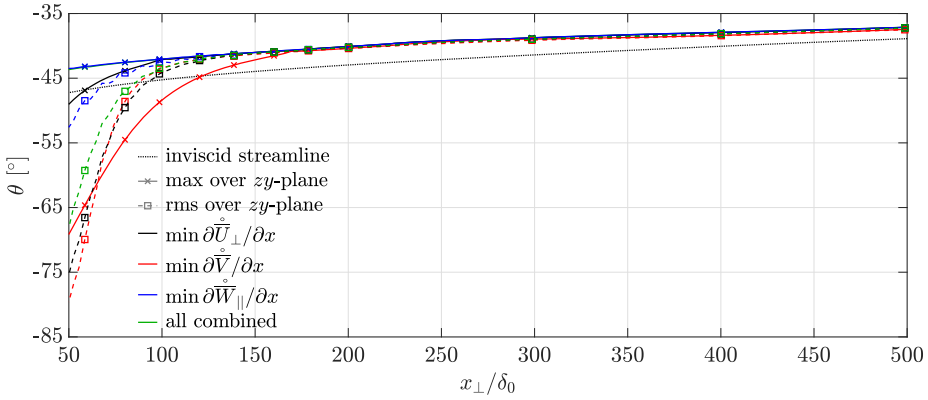

Fig. 4. Angle from the leading-edge-orthogonal $x_\perp$-direction to the inviscid streamline and the directions that minimize the maximum value within the zy-plane (crosses) or root-mean-square value across the zy-plane (squares) of the x-derivative of $\mathring{\overline{U}}_\perp$, $\mathring{\overline{V}}$, $\mathring{\overline{W}}_{||}$, or their Pythagorean sum (this sum of the components is marked as 'all combined'). All collapse on the direction of the crossflow vortex's vortical axis.

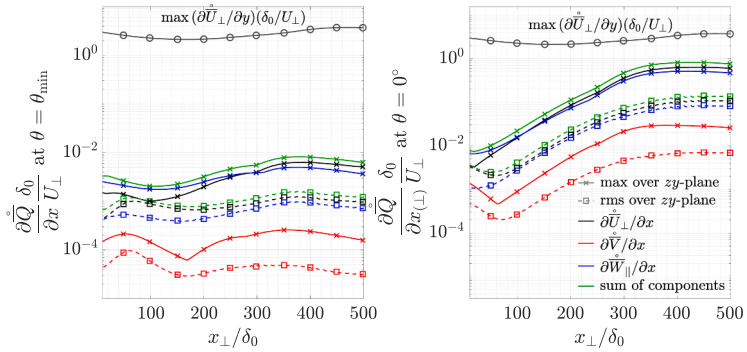

Fig. 5. Different measures of the x-derivatives (max or r.m.s. over the zy-plane of $\mathring{\overline{U}}_\perp$, $\mathring{\overline{V}}$, $\mathring{\overline{W}}_{||}$, or their combination) as evaluated with $\theta=\theta_{\min}$ and 0° ($x=x_\perp$). By using the non-orthogonal coordinate, the x-derivatives are reduced by about two orders of magnitude.

the quantity:

$$\sqrt{\iint\left\{\left(\frac{\partial\mathring{\overline{U}}_\perp}{\partial x}\right)^2+\left(\frac{\partial\mathring{\overline{V}}}{\partial x}\right)^2+\left(\frac{\partial\mathring{\overline{W}}_{||}}{\partial x}\right)^2\right\}\mathrm{d}y\,\mathrm{d}z}. \tag{10}$$

In Figs. 4 and 5, quantities corresponding to the θ-value that minimizes the expression in Eq. (10) are indicated with green squares and marked as corresponding to 'all [components] combined'. Similarly, the green circles in these figures correspond to the θ-value that minimizes:

$$\max_{z,y}\left\{\sqrt{\left(\frac{\partial\mathring{\overline{U}}_\perp}{\partial x}\right)^2+\left(\frac{\partial\mathring{\overline{V}}}{\partial x}\right)^2+\left(\frac{\partial\mathring{\overline{W}}_{||}}{\partial x}\right)^2}\right\}. \tag{11}$$

Lastly, Fig. 5 demonstrates how the measures of the x-derivatives corresponding to $\theta=\theta_{\min}$ are about two orders of magnitude smaller than the $x_\perp$-derivatives. The same figure also demonstrates that these x-derivatives are more than two orders of magnitude smaller than the principal shear associated to the leading-edge-orthogonal velocity component, $\partial\mathring{\overline{U}}_\perp/\partial y$.

2.4. Non-orthogonal plane-marching approach

Recall that $\mathring{\overline{Q}}$, the steady base flow distorted by the stationary crossflow vortex, evolves slowly in x, and q' is the perturbation thereto, which is further decomposed as follows:

$$q'(x,y,z,t)=\tilde{q}(x,y,z)\,\mathrm{e}^{\mathrm{i}\left(\int^x\alpha(\bar{x})\mathrm{d}\bar{x}-\omega t\right)}+c.c., \tag{12}$$

where $\tilde{q}$ is the perturbation's shape function, α the streamwise wavenumber, and ω the angular frequency, which is related to the cyclic frequency f through $\omega=2\pi f$. Furthermore, $\bar{x}$ represents the dummy integration variable corresponding to x, and $c.c.$ denotes the complex conjugate. Note that $-\alpha_i$ represents the exponential growth in the x-direction, while $-\alpha_i\sec\theta$ represents the exponential growth in the $x_\perp$-direction, under the restriction that q' is periodic in $z_{(||)}$.

Advantage is taken of the slow development of the distorted base-flow variables in x by specifying a slow development of the shape function and wavenumber in x. Repeatedly differentiating Eq. (12) with respect to x, one obtains:

$$\frac{\partial q'}{\partial x}=\left(\frac{\partial\tilde{q}}{\partial x}+\mathrm{i}\alpha\,\tilde{q}\right)\mathrm{e}^{\cdots}+c.c.; \tag{13a}$$

$$\frac{\partial^2 q'}{\partial x^2}=\left(\frac{\partial^2\tilde{q}}{\partial x^2}+2\mathrm{i}\alpha\frac{\partial\tilde{q}}{\partial x}-\alpha^2\,\tilde{q}+\mathrm{i}\frac{\mathrm{d}\alpha}{\mathrm{d}x}\tilde{q}\right)\mathrm{e}^{\cdots}+c.c. \tag{13b}$$

By using ansatz (12) in the linearized Navier-Stokes equations for incompressible flow, one obtains:

$$\frac{\tilde{D}\tilde{u}_\perp}{\tilde{D}t}=\tilde{R}\,\mathring{\overline{U}}_\perp-\left(\Omega_p\Omega_1\frac{\partial\tilde{p}}{\partial x}+\mathrm{i}\alpha\,\tilde{p}\right)\sec\theta+\frac{\partial\tilde{p}}{\partial z}\tan\theta+\frac{\tilde{L}\tilde{u}_\perp}{Re}; \tag{14a}$$

$$\frac{\tilde{D}\tilde{v}}{\tilde{D}t}=\tilde{R}\,\mathring{\overline{V}}-\frac{\partial\tilde{p}}{\partial y}+\frac{\tilde{L}\tilde{v}}{Re}; \tag{14b}$$

$$\frac{\tilde{D}\tilde{w}_{||}}{\tilde{D}t}=\tilde{R}\,\mathring{\overline{W}}_{||}-\frac{\partial\tilde{p}}{\partial z}+\frac{\tilde{L}\tilde{w}_{||}}{Re}; \tag{14c}$$

$$0=\left(\Omega_1\frac{\partial\tilde{u}_\perp}{\partial x}+\mathrm{i}\alpha\,\tilde{u}_\perp\right)\sec\theta+\frac{\partial\tilde{v}}{\partial y}+\frac{\partial\tilde{w}_{||}}{\partial z}-\frac{\partial\tilde{u}_\perp}{\partial z}\tan\theta, \tag{14d}$$

where $\tilde{D}/\tilde{D}t$, $\tilde{R}$, and $\tilde{L}$ represent the material-derivative operator, the Reynolds stress terms, and the transformed Laplacian, respectively:

$$\frac{\tilde{D}}{\tilde{D}t}=-\mathrm{i}\omega+\mathring{\overline{U}}_\perp\sec\theta\left(\Omega_1\frac{\partial}{\partial x}+\mathrm{i}\alpha\right)+\mathring{\overline{V}}\frac{\partial}{\partial y}+\left(\mathring{\overline{W}}_{||}-\mathring{\overline{U}}_\perp\tan\theta\right)\frac{\partial}{\partial z}; \tag{14e}$$

Table 1
Key to what Ω-parameters to use for each approach.

Approach	Abbrev.	Ω_b	Ω_1	Ω_p	Ω_2
(Consistent) Local	L	0	0	–	0
Quasi-Local	QL	1	0	–	0
Plane-Marching (stabilized)	PM	1	1	0	0
Plane-Marching (not stabilized)	PM	1	1	1	0

$$-\tilde{R} = \Omega_b \tilde{u}_\perp \sec\theta \frac{\partial}{\partial x} + \tilde{v}\frac{\partial}{\partial y} + \left(\mathrm{i}\tilde{w}_{||} - \tilde{u}_\perp \tan\theta\right)\frac{\partial}{\partial z}; \tag{14f}$$

$$\begin{aligned}\tilde{L} = {} & \sec^2\theta\left(\Omega_2\frac{\partial^2}{\partial x^2} + 2\mathrm{i}\alpha\Omega_1\frac{\partial}{\partial x} - \alpha^2 + \mathrm{i}\Omega_1\frac{\mathrm{d}\alpha}{\mathrm{d}x} - \Omega_b\frac{\mathrm{d}\theta}{\mathrm{d}x_\perp}\frac{\partial}{\partial z} + \frac{\partial^2}{\partial z^2}\right) \\ & + \sec\theta\tan\theta\left(\Omega_b\frac{\mathrm{d}\theta}{\mathrm{d}x_\perp}\left(\Omega_1\frac{\partial}{\partial x} + \mathrm{i}\alpha\right) - 2\Omega_1\frac{\partial^2}{\partial x\,\partial z} - 2\mathrm{i}\alpha\frac{\partial}{\partial z}\right) + \frac{\partial^2}{\partial y^2}.\end{aligned} \tag{14g}$$

Note that Eqs. (14a) through (14c), while expressing functions in the nonorthogonal (x-, y-, z-)coordinates, still represent the equations for the perturbation momenta in the $x_\perp$-, y-, and $z_{||}$-directions. Although the velocity components could also be transformed, it is convenient to solve for the orthogonal $\tilde{u}_\perp$-component with the aim of comparing results against the DNS without further post-processing transformations. Several terms are multiplied with symbols of the form $\Omega_{\{b,1,p,2\}}$ in order to make explicit which terms are kept or dropped corresponding to the considered stability approach, see Table 1; this will be further elaborated in the next paragraph. Lastly, note that α naturally depends on x by ansatz (12); the angle θ, however, is most naturally defined in terms of $x_\perp$. Accounting for $\mathrm{d}\theta/\mathrm{d}x_\perp$ is necessary, given its potentially large magnitude (although, in the present study, it does not exceed $1°/\delta_0$).

The first derivatives with respect to x of the distorted base flow $\mathring{\overline{Q}}$ and perturbation shape functions $\tilde{q}$ are assumed to be small, following the slow-evolution assumption. Second x-derivatives are therefore regarded as negligibly small. For this reason, the first term in the first parentheses of (14g) will be dropped in the stability analyses ($\Omega_2 = 0$, $\Omega_1 = \Omega_b = 1$). Dropping this term parabolizes the system of equations with respect to the x-direction and enables solving for the three-dimensional solutions by marching a set of two-dimensional shape functions in the x-direction if the system's residual ellipticity is negligible [31]. The resulting system of equations constitutes the plane-marching Parabolized Stability Equations (plane-marching PSE). There are other terms in the equations that qualify as negligibly small under the aforementioned assumptions, e.g. products of x-derivatives of the shape functions and distorted base-flow quantities and x-derivatives that are divided by the Reynolds number. However, in the present formulation of the plane-marching PSE, these terms are retained and hence are not multiplied with Ω_2. Although the resulting formulation is formally inconsistent, these small terms were not observed to have a negative impact on achieving convergence of the auxiliary condition mentioned in Section 2.5. Moreover, we argue that retaining these terms, even if negligibly small, promises a better comparison against the DNS, if only because the DNS retains all terms. Lastly, we note that retaining or even adding new negligibly small terms is not uncommon: the stabilization procedure outlined in Section 2.7 relies on the latter.

The 'quasi-local' problem is obtained upon dropping all other x-derivatives of the perturbation shape functions and the $\mathrm{d}\alpha/\mathrm{d}x$-term in $\tilde{L}$ ($\Omega_2 = \Omega_1 = 0$, $\Omega_b = 1$); the x-derivatives of $\mathring{\overline{Q}}$ and $x_\perp$-derivative of θ are kept in order to account for as many physical effects as possible. Finally, the (proper/consistent) 'local' problem is obtained by dropping x-derivatives of all quantities ($\Omega_2 = \Omega_1 = \Omega_b = 0$). This 'local' formulation is here also called consistent, because the distorted base-flow, disturbance, and coordinate (i.e. θ) variables are treated equally. The parameter Ω_p in Eq. (14a) will be discussed in Section 2.7.

Although this is standard in the literature, referring to the aforementioned assumptions as the 'parallel-flow assumption' is a misnomer for the presently considered approaches, because they do not require dropping $\mathring{\overline{V}}$. Upon stating the incompressible continuity equation for the distorted base flow in both non-orthogonal coordinates and non-orthogonal velocity components (see Eq. (9)):

$$\frac{\partial\mathring{\overline{U}}}{\partial x} + \frac{\partial\mathring{\overline{V}}}{\partial y} + \frac{\partial\mathring{\overline{W}}}{\partial z} = 0. \tag{15}$$

The assumptions render $\partial\mathring{\overline{U}}/\partial x$ small, but $\partial\mathring{\overline{W}}/\partial z$ is $O(1)$. Hence, $\mathring{\overline{V}}$ should not be dropped from the equations; neither for the plane-marching, nor the quasi-local, nor the local approach. Bonfigli and Kloker [10, Fig. 20] and Groot et al. [32] demonstrate that the in-plane flow components ($\mathring{\overline{V}}$ and $\mathring{\overline{W}}_{(||)}$) play a crucial role for the growth rates of all instability modes of crossflow vortices.

2.5. Boundary, initial, and auxiliary conditions

The system of non-orthogonal, plane-marching PSE, Eq. (14), is closed with boundary, initial, and auxiliary conditions. Periodic boundary conditions are imposed at the spanwise boundaries ($z = -\lambda_z/2$ and $z = \lambda_z/2$, where $\lambda_z = \lambda_{z_{||}} = 7.5$ mm is the spanwise wavelength of the crossflow vortex). No-slip conditions are imposed at the wall ($y = 0$) and at the free-stream boundary ($y = y_{\max} = 25.86\delta_0$, about 5 times the maximum height of the 90 % streamwise velocity contour at the leading-edge-orthogonal outflow boundary of the domain, where δ_0 is the inlet boundary-layer thickness at $x_\perp = 0$). The y-momentum equation is used as a compatibility condition for the pressure at wall and free-stream boundaries. The quasi-local eigenvalue problem is solved in spatial form (for complex α, upon specifying a value of ω) in order to obtain initial conditions. The solutions to the quasi-local problem ($\Omega_2 = \Omega_1 = 0$, $\Omega_b = 1$) are preferred over those of the local problem ($\Omega_2 = \Omega_1 = \Omega_b = 0$)

Ansatz (12) in itself does not guarantee that the x-derivative of the perturbation shape functions $\tilde{q}$ is small; the x-dependence of both α and $\tilde{q}$ in ansatz (12) is leveraged for this purpose. Given a reasonable initial guessed solution for a given $x_\perp$-station, the x-derivative of the shape functions is iteratively minimized by updating α with the following auxiliary condition:

$$\alpha^{k+1} = \alpha^k - \mathrm{i}\frac{\iint \vec{\tilde{\mathbf{q}}}^{\mathrm{H}}\mathcal{M}\dfrac{\partial\vec{\tilde{\mathbf{q}}}}{\partial x}\,\mathrm{d}y\,\mathrm{d}z}{\iint \vec{\tilde{\mathbf{q}}}^{\mathrm{H}}\mathcal{M}\vec{\tilde{\mathbf{q}}}\,\mathrm{d}y\,\mathrm{d}z}; \quad \mathcal{M} = \begin{bmatrix}1 & & & 0\\ & 1 & & \\ & & 1 & \\ 0 & & & 0\end{bmatrix}, \tag{16}$$

where $\vec{\tilde{\mathbf{q}}}^{\mathrm{H}} = [\tilde{u}_\perp^{\mathrm{H}}\ \tilde{v}^{\mathrm{H}}\ \tilde{w}_{||}^{\mathrm{H}}\ \tilde{p}^{\mathrm{H}}]$ and the superscript H indicates Hermitian transposition. The perturbation-pressure contribution is dropped (via $\mathcal{M}$) from this condition, because it is directly coupled to the velocity perturbations for incompressible conditions. This condition was deemed satisfied when relative α-differences were recorded to drop below the threshold: $|\alpha^{k+1} - \alpha^k|/|\alpha^{k+1}| \leq 2.2 \times 10^{-10}$.

2.6. Discretization

The plane-marching PSE and boundary conditions are discretized by using finite differences. Sixth order, central differences are used in z and y, while fixing the stencil width and moving the evaluation point for derivatives toward a given boundary when necessary. A BiQuadratic mapping [34, Section 3.1.4, pp. 70–71] is used in $z_{(||)}$ to produce an approximately uniform distribution. That is, one-third of the collocation nodes is placed within the intervals $z/\lambda_z \in [-1/2, z_{i1}]$, $[z_{i1}, z_{i2}]$, and $[z_{i2}, 1/2]$, while we set $(z_{i1}, z_{i2})/\lambda_z = (-1, 1)/6$. Another BiQuadratic mapping is used in y to highly cluster the grid around the shear layer of interest. Similarly, one-third of the collocation nodes is placed within the intervals $y/\delta_0 \in [0, y_{i1}]$, $[y_{i1}, y_{i2}]$, and $[y_{i2}, y_{\max}]$, while we adopt $(y_{i1}, y_{i2}, y_{\max})/\delta_0 = (2.5, 5, 25.86)$. The resulting grid is shown in Fig. 6. Upon using a Chebyshev Gauss-Lobatto node-distribution in the computational ξ-domain with $\xi \in [-1, 1]$ [34, Section 3.1.1, pp. 59–61], nodes are clustered toward the boundaries to avoid the Runge phenomenon. The wall-normal mapping parameters were chosen to maximize the resolution for the most unstable $x_\perp$-instance of the most-amplified mode as

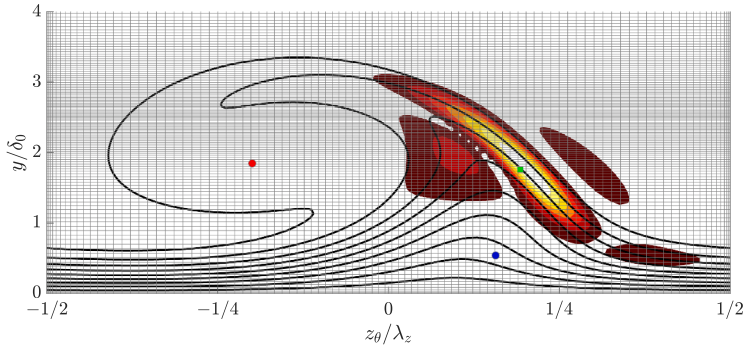

Fig. 6. Grid resolving *type*-I secondary instability mode at $x/\delta_0 = 425$ and 6 kHz as computed with the local approach. Grid (gray lines), isolevels of $|\tilde{u}_\perp|$ (filled contours; 1/8, 2/8, …7/8 of maximum) and $\overset{\circ}{U}_\perp$ (solid lines: 10 %, 20 %, …90 % of maximum). Saddle (green square) and centers (red circle: anti-clockwise; blue circle: clockwise rotation) generated by the non-orthogonal $\overset{\circ}{V}$- and $\overset{\circ}{W}$-components: $\overset{\circ}{V} = \overset{\circ}{W} = 0$. To distinguish saddles from centers, we use the λ_2-vortex-identification criterion [33, vortex: $\lambda_2 < 0$]; the streamwise vorticity component then determines the direction of rotation of the in-plane flow around the centers. The *type*-I mode is typically forced onto the saddle formed by the in-plane flow [32].

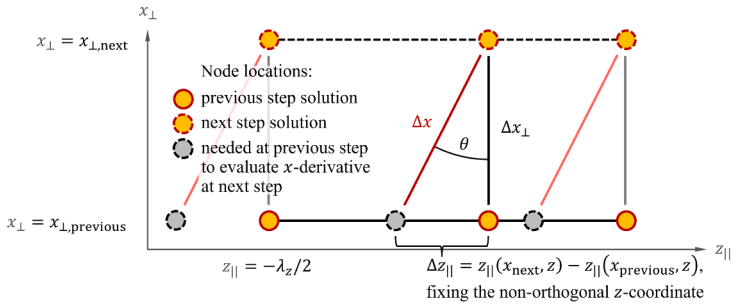

Fig. 7. Illustration of how the previous step solution must be interpolated onto a grid shifted in the $z_{||}$-direction, in order to evaluate the x-derivative at the next step.

computed with the local approach (*type*-I with maximal $-\alpha_i \sec\theta$ in $x_\perp$ for $f = 5.2$ kHz; $|\Delta\alpha_i/\alpha_i| = \mathcal{O}(10^{-5})$ or less, upon reducing the number of nodes by 10 % in each direction). A high number of nodes is used in the z- and y-directions ($N_z = 100$ and $N_y = 200$) in order to provide highly accurate solutions over the entirety of the domain in the streamwise direction. Backward differences (backward Euler) are used in x. Usually, steps of $\Delta x_\perp/\delta_0 = 1$ are taken, so that $\Delta x/\delta_0 = \sec\theta(x_\perp)$; this was found to produce converged results with respect to $x_\perp$-resolution, which will be addressed among the results in Section 3.2. Outstepping residual ellipticity will be further discussed in Section 2.7. All integrals over spatial coordinates are computed using numerical approaches with the same or higher orders of accuracy as the finite differences in the corresponding directions. The local, spatial eigenvalue problem is solved using the Arnoldi algorithm.

At each step, the solution is evaluated at the same $z_{||}$-domain, spanning $z_{||}/\lambda_z \in [-1/2, 1/2]$, to conform with the domain used in the DNS for the distorted base flow and achieve the best incorporation of the in-plane derivatives of distorted base-flow quantities. Hence, the backward x-derivative queries the previous step solution at locations where it is usually unavailable; see Fig. 7. The solution at the previous step must therefore be interpolated onto a shifted instance of the grid in the $z_{||}$-direction. The interpolation is done with the same order as the finite differences used to discretize the z-dimension. Furthermore, the solution's periodicity is leveraged to find solution values that are queried outside of the available $z_{||}$-domain.

2.7. Mitigation of residual-ellipticity

System (14) is referred to as a set of parabol*ized* stability equations, not parabolic, because dropping the second x-derivative term from $\tilde{L}$ leaves a residual ellipticity [31]. Li and Malik [35,36] showed that this prohibits solving the system with a marching technique if one makes too small a step, i.e. when $\Delta x < 1/|\alpha_r| = \lambda_x/2\pi$: 'a maximum of 2π steps per disturbance wavelength are allowed for the marching.' Thereby, this step-size restriction prohibits letting $\Delta x \to 0$ without further adjustments to the approach. To mitigate this problem, Haj-Hariri [37] proposed the removal of the term $\partial\tilde{p}/\partial x$ from Eq. (14a; $\Omega_p = 0$), which is similar to the approach proposed by Vigneron et al. [38]. Instead of *dropping* terms that could potentially have an important impact on the behavior of the solution, Andersson et al. [17] proposed to resolve the residual-ellipticity issue by *adding* asymptotically small terms instead.

In order to converge the plane-marching problem for a very small step size and while leaving $\Omega_p = 1$, we use the stabilization approach by Andersson et al. [17]. To concisely illustrate its implementation, system (14) and the (here all homogeneous) boundary conditions are first cast into the form:

$$\mathcal{B}\frac{\partial\vec{\tilde{\mathbf{q}}}}{\partial x} = \mathcal{A}\vec{\tilde{\mathbf{q}}} \tag{17}$$

where $\vec{\tilde{\mathbf{q}}}$ is defined under Eq. (16) and $\mathcal{A}$ and $\mathcal{B}$ are operators containing all distorted base-flow variables and derivative operators for each equation and a guess for the streamwise wavenumber, $\alpha^{(k)}$, at the next x-station. The *unmodified* approach proceeds to solve this equation with a backward Euler approach:

$$\left[\frac{\mathcal{B}}{\Delta x} - \mathcal{A}\right]\vec{\tilde{\mathbf{q}}}\Big|_{\text{next } x} = \frac{\mathcal{B}}{\Delta x}\vec{\tilde{\mathbf{q}}}\Big|_{\text{previous } x} \tag{18}$$

for $\vec{\tilde{\mathbf{q}}}$ at the next x-station and then the guess for α is updated with auxiliary condition (16). This process is repeated until the convergence criterion on α, mentioned under Eq. (16), is satisfied. Instead of Eq. (18), Andersson et al. propose solving:

$$\mathcal{B}\frac{\partial\vec{\tilde{\mathbf{q}}}}{\partial x} = \mathcal{A}\vec{\tilde{\mathbf{q}}} + s\mathcal{A}\frac{\partial\vec{\tilde{\mathbf{q}}}}{\partial x}; \tag{19}$$

$$\left[\frac{\mathcal{B}}{\Delta x}-\left(1+\frac{s}{\Delta x}\right)\mathcal{A}\right]\vec{\tilde{\mathbf{q}}}\Big|_{\text{next } x}=\frac{\mathcal{B}-s\mathcal{A}}{\Delta x}\vec{\tilde{\mathbf{q}}}\Big|_{\text{previous } x} \tag{20}$$

where s is a stabilization length scale, that adjusts the step-size criterion by Li and Malik [35,36] for (orthogonal, line-marching) PSE to: $\Delta x > |\alpha_r|^{-1} - 2s$. That is, any step size $\Delta x \to 0$ can be used to successfully solve the equations by marching upon using:

$$s > \frac{1}{2}\left(\frac{1}{|\alpha_r|}-\Delta x\right)=\frac{1}{2}\left(\frac{1}{|\alpha_r|\sec\theta}-\Delta x_\perp\right)\sec\theta. \tag{21}$$

Such an s always exists for disturbances with a finitely long streamwise wavelength ($\alpha_r \neq 0$), but s is moreover required to be small in order for the added term in Eq. (19), $s\mathcal{A}\partial\vec{\tilde{\mathbf{q}}}/\partial x$, to be negligibly small under the slow-evolution assumption. While $\Delta x = \Delta x_\perp \sec\theta > \Delta x_\perp$ (which is desirable to outstep residual ellipticity), the wavelength scales by the same factor ($\lambda_x = 2\pi/\alpha_r = 2\pi\sec\theta/(\alpha_r \sec\theta) = \lambda_{x_\perp}\sec\theta$). Therefore, the non-orthogonal approach unfortunately does not lead to a favorable step-size criterion. In fact, a larger s-value is necessary to effectively stabilize the same step size in $x_\perp$, as exemplified by the factor $\sec\theta$ on the far right-hand side of Eq. (21).

The non-orthogonal formulation of the (plane-marching) PSE may satisfy an adjusted version of the stabilization criterion, other than the version presented as inequality (21), which is strictly valid for the orthogonal formulation of (line-marching) PSE. However, the stabilization approach was found to be an effective approach to stabilize solutions whenever the unadjusted plane-marching algorithm diverged in this study. The stabilization length s can be specified according to 2 approaches:

- fixed s: we can fix s in the streamwise direction to the smallest possible value as determined by trial and error (for this study it is also of $\mathcal{O}(\delta_0)$, i.e. the inlet boundary-layer thickness at $x_\perp = 0$), that still enables converging the plane-marching algorithm;
- fixed m: we can fix m in the streamwise direction and set:

$$s=\begin{cases}\frac{1}{2}\left(\frac{m}{|\alpha_r|}-\Delta x\right) & \text{if } m > |\alpha_r|\Delta x;\\ 0 & \text{otherwise.}\end{cases} \tag{22}$$

  That is, the stabilization is activated if we take more than $2\pi/m$ steps per wavelength. Inequality (21) is satisfied if $m \geq 1$ and has the added benefit that the stabilization approach is deactivated when the streamwise wavelength λ_x is or becomes long enough over a (potentially large) streamwise portion of the domain. Note that we only have access to a guessed value of α_r, because s must be set during the α-iterations with the auxiliary condition. The value of s is fixed after the third such iteration in order to avoid unnecessarily prolonging convergence.

It will be shown that converged solutions can be obtained with both approaches (fixing either s or m). In this paper, the fixed-s approach is used predominantly, i.e. s is fixed to the smallest value that yielded converged results. If a smaller s-value is used, the α^k-iteration scheme with the auxiliary condition (16) does not converge and usually causes extremely negative α_i-values (without the oscillations shown by Li and Malik [36, Fig. 2]).

2.8. Note on computational cost

The non-orthogonal plane-marching approach calculates linear instability mechanisms with high fidelity in an efficient manner in terms of computational cost. That way, it is the ideal approach to accompany and guide DNS studies of the full non-linear disturbance evolution.

In having reduced the disturbance problem to marching a two-dimensional plane, the required memory is small enough for modern desktop computers that multiple frequencies can be computed in parallel: about 4GBs RAM to perform a shape-function update for the presently used resolution of $(N_z, N_y) = (100, 200)$ and 6th-order finite differences.

Although the time duration required to compute the instability modes from their first neutral point throughout the domain of interest can be highly variable from case to case (mode type, frequency, downstream position, etc.), we can give an approximate indication based on the computations performed for the present article. For the presently used resolution of $(N_z, N_y) = (100, 200)$ and 6th-order finite differences, a single α^k-iteration of the problem typically takes about 15 s on a personal computer. With a requirement of 4–9 α^k-iterations per $\Delta x_\perp$-step (typically more if stabilization is activated), it takes between 8.3 and 18.8 h to march a solution for a given frequency all the way from $x_\perp = 0$ to $500\delta_0$ with $\Delta x_\perp = \delta_0$. Solving the local or quasi-local eigenvalue problem with the Arnoldi algorithm, which is necessary to yield initial conditions for the plane-marching anyway, typically takes about 42 s to step a solution across the $x_\perp$ and frequency space on a personal computer. Hence, these approaches produce initial estimates of the most-amplified frequency most quickly (stepping from $x_\perp = 0$ to $500\delta_0$ with $\Delta x_\perp = \delta_0$ in about 5.8 h). For this reason, we recommend focusing the plane-marching approach on checking the most-amplified disturbances after an initial, broader explorative sweep is performed with a (quasi-)local approach.

Although the plane-marching approach takes a long time to run relative to traditional stability methods, especially compared to the line-marching PSE approach, conclusive results are generated within 24 h. This is still a very short time versus DNS, which took about 900,000 CPU hours (on 2048 cores with 1.8GB RAM per core) to run for the presently reported cases. Thus, besides yielding comparable results *efficiently*, the combined stability approaches moreover rendered the DNS campaign *effective*.

3. Results

The results will commonly be expressed in terms of N-factors, which represent the natural logarithm of the disturbance amplitude compared to its value at the neutral point:

$$N(x_\perp) = -\int_{x_{\perp,n}}^{x_\perp}\alpha_i(\bar{x})\sec(\theta(\bar{x}))\mathrm{d}\bar{x}+\frac{1}{2}\ln\left(\frac{\tilde{E}(x_\perp)}{\tilde{E}(x_{\perp,n})}\right) \tag{23}$$

where $\bar{x}$ is the dummy integration variable equivalent of $x_\perp$, $x_{\perp,n}$ corresponds to the neutral point, where $\mathrm{d}N/\mathrm{d}x = 0$, and finally:

$$\tilde{E}(x_\perp)=\int_{-\lambda_z/2}^{\lambda_z/2}\int_0^{y_{\max}}\left(|\tilde{u}_\perp(x_\perp,y,z_{||})|^2+|\tilde{v}|^2+|\tilde{w}_{||}|^2\right)\mathrm{d}y\,\mathrm{d}z_{||} \tag{24}$$

is the kinetic energy associated to the shape functions. Here, $y_{\max}$ is the height of the domain boundary.

3.1. Overview

An overview of the results, as computed for a broad range of frequencies and streamwise locations for all instability modes, is shown in Fig. 8. To be concise, we limit our reported results to modes that achieve the maximum amplification (maximum N *across* $x_\perp/\delta_0 \in [0, 500]$) for each frequency within the considered frequency band from 0 to 15 kHz. The main solution parameters associated to the most unstable (maximum $-\alpha_i\sec\theta$ in $x_\perp$) and neutral ($\alpha_i = 0$) instances corresponding to the most amplified frequency (maximum N *at* $x_\perp/\delta_0 = 500$) are given in Tables 2 and 3, respectively. As is commonly reported in the literature [4,5], the *type*-I & -II modes are most amplified for much higher frequencies (6 & 8 kHz, resp.) than the *type*-III mechanism (500 Hz). The *type*-III mechanism has more than one neutral point for frequencies between 700 Hz and 1.05 kHz, approximately, depending on the considered method. Whereas the N-factors for the (quasi-)local approaches are calculated starting form the most upstream neutral point, plane-marching results are computed starting either from the most upstream (crosses) or the third neutral point in the downstream direction (pluses).

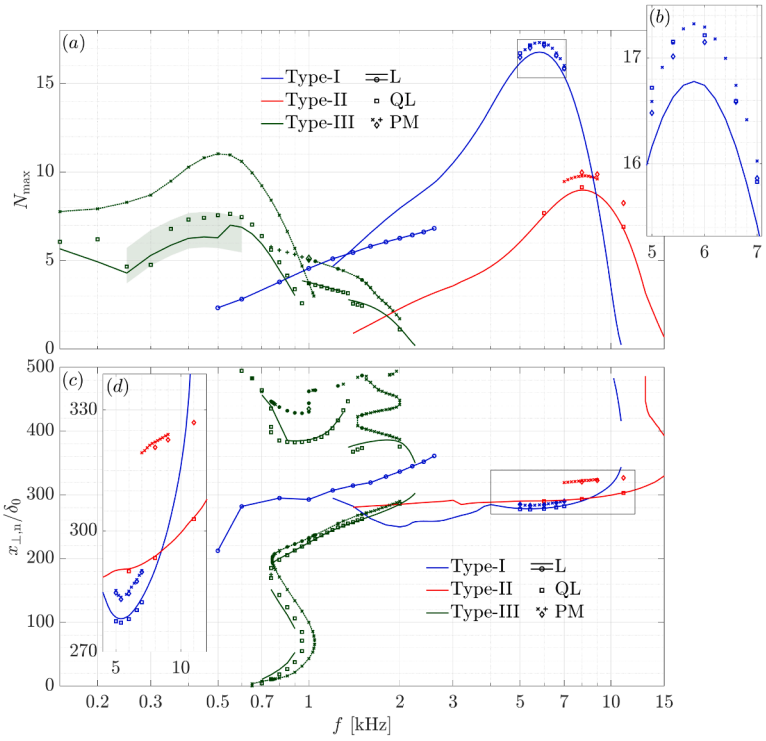

Fig. 8. (*a*,*b*) Maximum N-factor for $x_\perp/\delta_0 \in [0, 500]$ and (*c*,*d*) neutral points $x_{\perp,n}$ for the *type*-I (blue), -II (red), and -III (green) instability mechanisms as computed with the local (L, solid lines: unmarked and with circles), quasi-local (QL, squares), and plane-marching (PM, crosses: $\Omega_p = 0$; pluses: $\Omega_p = 0$ initialized from the third neutral point (when overlapping crosses, pluses appear as filled circles); diamonds: $s = \delta_0, 0, 2\delta_0$ for *type*-I, -II, and -III, respectively) approaches. Two instances of the *type*-I instability mechanism were found: one instance is shown as the solid blue line without markers and the other as the solid blue line with circles. Shaded region: crude uncertainty indication for the *type*-III N-factors as computed with the local approach. Insets (*b*,*d*) display the frequency on a linear scale.

Fig. 8 and Tables 2 and 3 demonstrate that stabilizing the plane-marching approach with the method of Andersson et al. [17] ($s > 0$; diamonds in Fig. 8) or removing the $\partial\tilde{p}/\partial x$-term (setting $\Omega_p = 0$; crosses and pluses in Fig. 8) produces practically identical results for the present conditions.

Results as computed with the local approach are shown with solid lines in Fig. 8. Two sets of solid blue lines denote two mode families that we attributed to the *type*-I instability mechanism. The second instance of the *type*-I instability mode, as found for low frequencies ($f < 3$ kHz) is shown as a solid blue line with circles, while the other instance corresponds to the solid blue line without markers. Both modes are identified as a *type*-I instance, because their eigenfunctions are similar to that shown in Fig. 6, i.e., they overlap the saddle in the in-plane flow; and their growth rate is driven dominantly by the spanwise ('shoulder') shear layer, e.g. by $\partial\breve{\overline{U}}_\perp/\partial z$ as contained in the $\tilde{R}\,\breve{\overline{U}}_\perp$-grouping in Eq. (14a).

As also reported by Ambrosino et al. [15] for a crossflow vortex at a lower amplitude, the plane-marching results consistently yield larger maximum achieved N-factors than the corresponding local results. The present work shows that this conclusion holds for a broad range of frequencies for each instability mechanism. Despite the different amplification, the most-amplified frequency is found to be the same for the *type*-I and -II disturbances (up to the used frequency resolution of 200 Hz; allowing an uncertainty of 3.4 %). The approaches yield close most-amplified frequencies for the *type*-III instability mechanism, although the local approach struggles to clearly indicate a most-amplified frequency in that case. This is represented by the non-smooth increase in the green solid N_{max}-line for the local approach as seen in Fig. 8(*a*) from $f = 500$ to 550 Hz. We added a green shaded patch to indicate that the N-factors for the *type*-III instability mechanism are uncertain around $f = 500$ Hz as computed with the local approach. It is necessary to specify that these results were computed by using small enough $\Delta x_\perp$-steps to accurately resolve any relatively fast variations in the α-eigenvalues, which will be further supported in Section 3.2.

This uncertain behavior of the *type*-III mode hints that two α-eigenvalues achieve a close proximity in the complex α-plane, which is signified by a cusp-like behavior of, for example, the growth rate $-\alpha_i$ versus $x_\perp$ or f, see Briggs [39] and Huerre and Monkewitz [40,41]. This behavior is more typically encountered in the stability analysis of (laminar, undistorted) hypersonic boundary layers, see Fedorov and Tumin [42] and Tumin and Aizatulin [43]. Whenever α-eigenvalues come close, the disturbance description by a (quasi-)local approach is ambiguous: it is unclear which eigenvalue should be tracked in $x_\perp$. This issue cannot simply be solved by switching modes at the correct $x_\perp$-location for multiple, related reasons. First, the issue is challenging to identify without comparing against other approaches. For this reason, Fedorov and Tumin [42] conclude that the local approach should be abandoned for an initial-boundary-value problem in this circumstance, which, in the strictest sense, is equivalent to our unsteady DNS. Second, even upon using a small enough step ($\Delta x_\perp = \delta_0$) to adequately capture the quick (but finite) α-variations with the (quasi-)local approaches, one may still be 'picking the wrong mode'.

While close encounters of α-eigenvalues deserve a much deeper investigation in itself, we aim the present article's results at demonstrating how the plane-marching approach yields a significant, qualitative improvement over the local results in this circumstance. The plane-marching approach 'lets the differential equations decide' what (linear combination of) modes to track by projecting onto the full eigenbasis (not just selecting one eigenmode) whenever we invert Eqs. (18) or (19) for $\tilde{\mathbf{q}}|_{\text{next } x}$. We will focus our attention on the *type*-III instance at $f = 1$ kHz in the remainder of the article, because this frequency lies closer to a saddle point (the counterpart of a cusp in the α-solutions in the complex ω-plane [39,40]) and thus enables revealing how the

Table 2
Most unstable ($\max_{x_\perp}\{-\alpha_i \sec\theta\}$) *type*-I, -II, and -III mode characteristics at $f = 6$, 8, and 1 kHz, respectively, obtained with the local (L), quasi-local (QL), or plane-marching (PM) approach. Note that $\overline{U}_e$, λ_x, c_{ph}, and c_{g} are quantities that are aligned with the non-orthogonal x-direction, pointing along the crossflow vortex; θ allows transforming to the $x_\perp$-direction.

	Type-I (most unstable at $f = 6$ kHz)			
Approach	L	QL	PM	PM
Stabilization	–	–	$\Omega_p = 0$	$s = \delta_0$
$x_\perp/\delta_0$	425.01±1	418.04±1	433.93±1	433.93±1
θ (°)	−37.9	−38.0	−37.8	−37.8
$\overline{U}_e/U_\perp$	1.91	1.90	1.91	1.91
$-\alpha_i\delta_0 \sec\theta \times 10^2$	9.560	9.755	9.997	9.872
λ_x/δ_0	4.661	4.656	4.697	4.699
$c_{\text{ph}}/\overline{U}_e$ (%)	74.94	75.02	75.32	75.35
$c_{\text{g}}/\overline{U}_e$ (%)	79.33	79.12	78.82	78.79

	Type-II (most unstable at $f = 8$ kHz)			
Approach	L	QL	PM	PM
Stabilization	–	–	$\Omega_p = 0$	none: $s = 0$
$x_\perp/\delta_0$	347.06±1	347.06±1	378.99±1	378.01±1
θ (°)	−38.6	−38.6	−38.3	−38.3
$\overline{U}_e/U_\perp$	1.85	1.85	1.88	1.88
$-\alpha_i\delta_0 \sec\theta \times 10^2$	6.552	6.602	6.953	7.057
λ_x/δ_0	4.084	4.087	4.072	4.071
$c_{\text{ph}}/\overline{U}_e$ (%)	89.95	90.01	88.64	88.63
$c_{\text{g}}/\overline{U}_e$ (%)	85.71	85.95	85.94	85.93

	Type-III (most unstable at $f = 1$ kHz)			
Approach	L	QL	PM	PM
Stabilization	–	–	$\Omega_p = 0$	$s = 2\delta_0$
$x_\perp/\delta_0$	304.92±1	302.01±1	313.03±1	313.03±1
θ (°)	−38.9	−38.9	−38.8	−38.8
$\overline{U}_e/U_\perp$	1.82	1.82	1.83	1.83
$-\alpha_i\delta_0 \sec\theta \times 10^2$	3.777	3.771	4.417	4.402
λ_x/δ_0	15.09	15.12	15.11	15.12
$c_{\text{ph}}/\overline{U}_e$ (%)	42.23	42.37	42.17	42.19
$c_{\text{g}}/\overline{U}_e$ (%)	41.75	41.63	42.18	–

Table 3
Neutral ($\min_{x_\perp}|\alpha_i|$ available) *type*-I, -II, and -III mode characteristics at $f = 6$, 8, and 1 kHz, respectively, obtained with the local (L), quasi-local (QL), or plane-marching (PM) approach. Note that $\overline{U}_e$, λ_x, c_{ph}, and c_{g} are quantities that are aligned with the non-orthogonal x-direction, pointing along the crossflow vortex; θ allows transforming to the $x_\perp$-direction.

	Type-I (neutral at $f = 6$ kHz)			
Approach	L	QL	PM	PM
Stabilization	–	–	$\Omega_p = 0$	$s = \delta_0$
$x_\perp/\delta_0$	278.99±1	278.99±1	284.99±1	284.02±1
θ (°)	−39.2	−39.2	−39.1	−39.1
$\overline{U}_e/U_\perp$	1.81	1.80	1.81	1.81
$\alpha_i\delta_0 \sec\theta \times 10^4$	4×10^{-3}	3.9	1.7	6.0
λ_x/δ_0	4.580	4.589	4.533	4.538
$c_{\text{ph}}/\overline{U}_e$ (%)	77.73	77.92	76.74	76.87
$c_{\text{g}}/\overline{U}_e$ (%)	79.34	83.39	81.20	81.41

	Type-II (neutral at $f = 8$ kHz)			
Approach	L	QL	PM	PM
Stabilization	–	–	$\Omega_p = 0$	none: $s = 0$
$x_\perp/\delta_0$	294.06±1	292.93±1	321.94±1	320.97±1
θ (°)	−39.0	−39.0	−38.8	−38.8
$\overline{U}_e/U_\perp$	1.82	1.82	1.84	1.84
$\alpha_i\delta_0 \sec\theta \times 10^4$	−7.9	10.9	2.8	−4.1
λ_x/δ_0	3.957	3.958	3.879	3.877
$c_{\text{ph}}/\overline{U}_e$ (%)	89.01	89.06	86.28	86.27
$c_{\text{g}}/\overline{U}_e$ (%)	84.87	84.94	81.44	81.10

	Type-III (neutral at $f = 1$ kHz)			
Approach	L	QL	PM	PM
Stabilization	–	–	$\Omega_p = 0$	$s = 2\delta_0$
$x_\perp/\delta_0$	224.97±1	224.97±1	231.98±1	231.98±1
θ (°)	−39.9	−39.9	−39.8	−39.8
$\overline{U}_e/U_\perp$	1.77	1.77	1.77	1.77
$\alpha_i\delta_0 \sec\theta \times 10^4$	0.11	1.2	2.9	−2.5
λ_x/δ_0	15.01	14.99	14.86	14.87
$c_{\text{ph}}/\overline{U}_e$ (%)	43.34	43.30	42.82	42.85
$c_{\text{g}}/\overline{U}_e$ (%)	40.21	40.16	39.26	–

plane-marching approach demonstrates improvement over both the local and quasi-local approaches when verifying the results against DNS in Section 3.3.

Another important take-away from Fig. 8(*c*,*d*) is that the neutral points for the *type*-II instability mechanism as computed with the plane-marching approach lie significantly farther downstream than those computed with both the quasi-local and local approaches. Although this also occurs to a minor extent in the *type*-I and -III disturbances, the effect is uniquely emphasized in the *type*-II disturbance. This will be addressed in detail in Section 3.4. First, however, we will address grid convergence and verification against line-marching PSE in Section 3.2.

3.2. Grid convergence study & verification against line-marching PSE

A convergence study is performed for all spatial dimensions. Besides N_z and N_y for the number of points spanning the spanwise and wall-normal extents of the domain, the number of points used to resolve the unit δ_0 in the $x_\perp$-direction will be denoted as $\delta_0/\Delta x$. Furthermore, the disturbances considered are the:

a. traveling crossflow (TCF) disturbance at 300 Hz ($\theta \equiv 0°$, $m = 1$);
b. *type*-III mode at 1 kHz ($\theta = \theta_{\min}$, $s = 2\delta_0$); and
c. *type*-I mode at 6 kHz ($\theta = \theta_{\min}$, $s = \delta_0$).

The (primary) TCF disturbance is computed by swapping the distorted base-flow quantities, $\breve{\overline{Q}} = \breve{\overline{Q}}(x_\perp, y, z_{||})$, for their undisturbed equivalents, $\overline{Q} = \overline{Q}(x_\perp, y)$, in system (14). The undisturbed base flow evolves slowly in the $x_\perp$-direction, hence the orthogonal approach ($\theta = 0°$) is appropriate in that case.

The quantities that were assessed are the streamwise wavenumber α_r and N-factor as evaluated at the end of the domain; with the latter assessing the solution behavior over the entirety of the domain. Relative errors are indicated for both quantities, defined by:

$$\left|\frac{\alpha_r - \alpha_{r,\text{ref}}}{\alpha_{r,\text{ref}}}\right| \quad \text{and} \quad \left|\frac{N - N_{\text{ref}}}{N_{\text{ref}}}\right|. \tag{25}$$

Besides the relevant $z_{||}$- and y-domains, the $x_\perp$-domain is considered starting from the initialization location closely upstream of the neutral point. In absence of analytical reference solutions, we work with reference solutions obtained at a high, though finite, resolution. Our convergence tests confirm, and also demonstrate to what extent, that the reference solutions we picked are grid independent.

The convergence results are shown in Fig. 9; the resolution used for the reference solution is indicated along the vertical axis of each panel. The expected convergence rates (6th order in y- and z-directions and 2nd order in x), as indicated with the dash-dotted lines, are retrieved in all directions for all disturbances, in both assessed quantities. The achieval of the rate in the $x_\perp$-direction for the *type*-I and -III disturbances is slightly hampered due to the size variation of the step in the non-orthogonal x-direction, as it depends on $\theta = \theta(x_\perp)$. This is exemplified

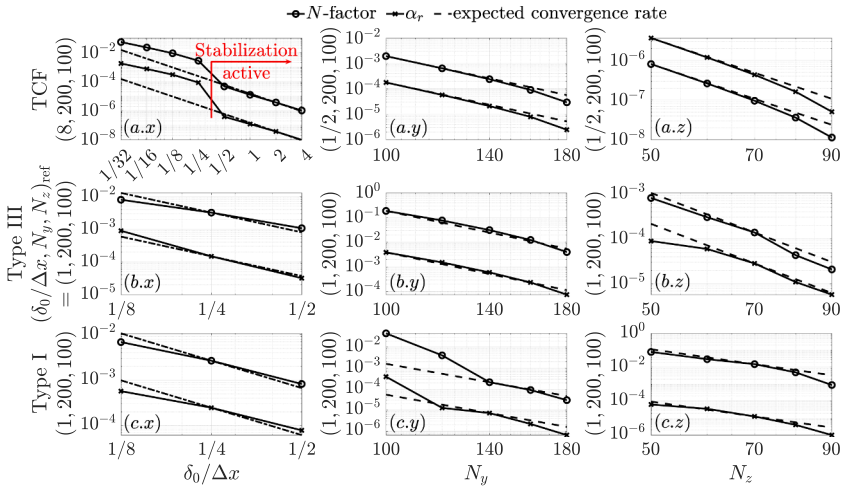

Fig. 9. Stability grid convergence study in relative error in the N-factor and α_r at the end of the available domain (solid lines) versus expected convergence rate: 6th order in y and z (dashed lines) and 2nd in x (dash-dotted lines). The resolution of the reference solution is indicated along each vertical axis, e.g. that for the x-resolution-convergence test for *type*-III $(b.x)$ was $(\delta_0/\Delta x, N_y, N_z)_{\text{ref}} = (1, 200, 100)$. $(a.x - z)$ Traveling crossflow instability at 300 Hz (computed with orthogonal coordinates, i.e. $\theta \equiv 0$, $m = 1$ for $\delta_0/\Delta x > 1/4$), $(b.x - z)$ *type*-III instability at 1 kHz ($s = 2\delta_0$), and $(c.x - z)$ *type*-I instability at 6 kHz ($s = \delta_0$).

by the matching of the rates for the TCF-solution with the orthogonal approach.

Upon having established grid-converged solutions, the TCF-solution is compared against line-marching PSE results in Fig. 10, see Casacuberta et al. [16] for more details on the latter approach. All quantities demonstrate a convincing match. Some minor differences remain distinguishable, because the line-marching approach uses a (Chebyshev pseudo-)spectral discretization in the wall-normal direction instead of the sixth-order finite differences used in the present work's plane-marching approach.

3.3. Verification against DNS

The DNS of the unsteady flow field represents full fidelity: in terms of non-linear dynamics and fully resolving all spatial and temporal scales relevant for the secondary disturbances. In this subsection, we will establish a match with the stability results in terms of the amplitude and growth rates on the one hand and the disturbance shapes on the other.

To compare the results against the DNS as closely as possible, we swap out the $\tilde{E}$-term in definition (23) of the N-factor with the wall-normal integral of the absolute value of the (fast) Fourier transform of the $\tilde{u}_\perp$ shape function in the z-direction:

$$|\tilde{u}_\perp|_{(1,j)}(x_\perp, y) = \left| \int_{-\lambda_z/2}^{\lambda_z/2} \tilde{u}_\perp(x_\perp, y, z_{||}) \mathrm{e}^{\mathrm{i}j\beta z_{||}} \, \mathrm{d}z_{||} \right| \tag{26a}$$

with $\beta = 2\pi/\lambda_z$, so to yield the amplitude measure:

$$A^{\tilde{u}_\perp}_{(1,j)}(x_\perp) = \int_0^{y_{\max}} |\tilde{u}_\perp|_{(1,j)}(x_\perp, y) \mathrm{d}y. \tag{26b}$$

The corresponding N-factors are defined as:

$$N^{\tilde{u}_\perp}_{(1,j)} = -\int_{x_{\perp,\mathrm{n}}}^{x_\perp} \alpha_i(\bar{x}) \sec(\theta(\bar{x})) \mathrm{d}\bar{x} + \ln\left(\frac{A^{\tilde{u}_\perp}_{(1,j)}(x_\perp)}{A^{\tilde{u}_\perp}_{(1,-1)}(x_{\perp,\mathrm{n}})} \right). \tag{27}$$

To compare against the DNS, the $N^{\tilde{u}_\perp}_{(1,j)}$-factors are divided by $\ln(10)$ and then shifted (all j-instances by the same additive value) such that the amplitude corresponding to $|\tilde{u}|_{(1,-1)}$ matches the DNS equivalent at a reference location. These reference locations are indicated by a vertical, dashed line in Figs. 11 and 13. The corresponding total, spatial growth rates are:

$$\gamma_{(1,j)}(x_\perp) = \frac{\mathrm{d}N^{\tilde{u}_\perp}_{(1,j)}}{\mathrm{d}x_\perp}. \tag{28}$$

The persistent '1' in the tuples $(1, j)$ references the (fundamental) frequency considered for the stability solutions: 6 kHz for *type*-I and 1 kHz for *type*-III. Upon comparing the growth rates, the results as computed with the quasi-local versus local approach, i.e. that respectively includes ($\Omega_b = 1$) or omits ($\Omega_b = 0$) the out-of-plane derivatives of the distorted base flow ($\partial\mathring{\overline{Q}}/\partial x$), are very similar. Hence the quasi-local results are omitted in the comparison of the amplitudes and growth rates.

The 6 kHz, *type*-I disturbance amplitudes (panels a,b) and growth rates (insets c,d), as computed with the stability approaches and DNS, are compared in Fig. 11. Growth rates closely agree in the range $x_\perp/\delta_0 \in [325, 380]$. The error incurred by the local approach versus the DNS is about twice as large as observed for the plane-marching approach; this could still be argued to be small and explains the success of the local approach. Fig. 11 appears to suggest that the local approach yields a result that is more amplified than the plane-marching equivalent, while the reverse is typically expected. This suggestion comes about because Fig. 11 only invokes the (Fourier transform of the) $\tilde{u}_\perp$-component. Fig. 8, which accounts for the total disturbance kinetic energy, unequivocally confirms that the result from the plane-marching approach is slightly more amplified than that of the local approach.

Although the plane-marching results book a quantitative improvement over the local results in the range $x_\perp/\delta_0 \in [325, 380]$ in this case, results corresponding to both approaches differ from the DNS at the upstream and downstream extremes of the considered domain. Both departures can be explained by the physics that are intentionally omitted from the presently considered stability approaches. Downstream of $x_\perp/\delta_0 = 380$, nonlinear effects likely cause the DNS amplitudes to saturate, while the stability results display unimpeded growth. Upstream of $x_\perp/\delta_0 = 325$, the stability results tend to neutral growth, while the DNS results do so at a much slower rate. This is likely a manifestation of transient growth, as attributed to the non-orthogonality of the secondary instability eigenmodes. Because the wall blowing and suction does not perfectly project onto a single eigenmode around its neutral point, some transient effect, including growth, is expected. This notion of transient growth was conjectured by Koch et al. [5] and confirmed by Wassermann and Kloker [9, see bottom of p. 71].

The disturbance shapes calculated with the stability approaches are compared to the DNS in Fig. 12. The DNS results represent the disturbance at a unique phase in time, while the stability results' phase can be freely shifted, because we solve for complex shape functions $\tilde{q}$ as per Eq. (12). Hence, the stability results' phase is shifted so as to have the real part of the shape functions achieve a maximum at the same position

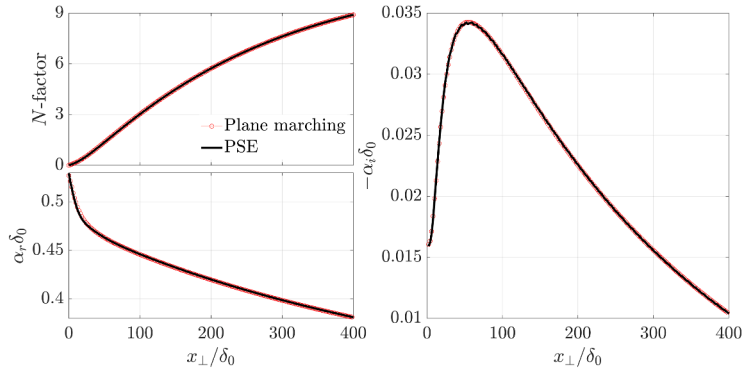

Fig. 10. Verification against (line-marching) PSE for the traveling crossflow instabiliy at 300 Hz using an orthogonal coordinate system.

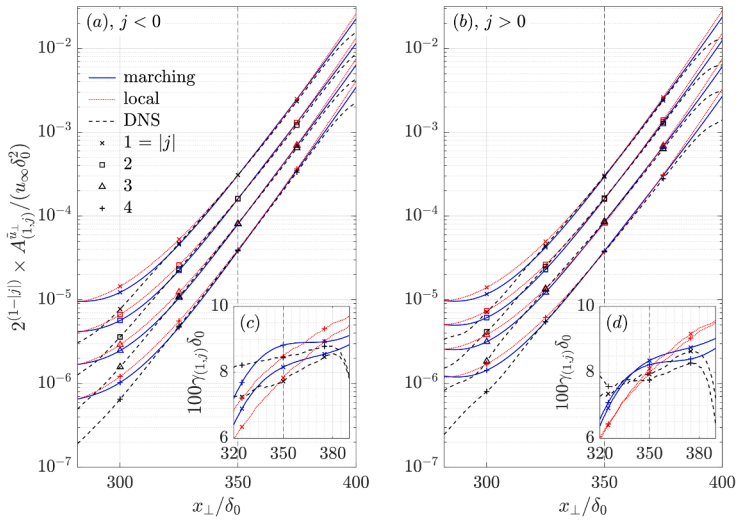

Fig. 11. Perturbation amplitudes (panels *a*,*b*) and growth rates (insets *c*,*d*) for the z-Fourier harmonics $|\tilde{u}|_{(1,j)}$ at 6 kHz attributed to the *type*-I instability mechanism (amplitude are scaled by a negative power of 2 to avoid overlapping lines). Amplitudes of the linear approaches' $|\tilde{u}|_{(1,-1)}$-harmonics match the DNS equivalent at $x_\perp/\delta_0 = 350$ (vertical dashed line).

in the zy-plane where the DNS result achieves the maximum amplitude. At 6 kHz, the disturbance shapes most closely agree with the DNS in the range $x_\perp/\delta_0 \in [300, 375]$, which extends farther upstream than where the growth rates match.

While the plane-marching results only book marginal improvements over the local results for the *type*-I disturbance at 6 kHz, a significant improvement is observed for the *type*-III disturbance at 1 kHz; the amplitude- and growth-rate comparison for which are shown in Fig. 13. Growth rates as computed with the plane-marching approach and the DNS match over practically the entire domain of interest. This is not the case for the local approach, however: the local-approach growth rates drop steeply around $x_\perp/\delta_0 = 400$. This drop appears so steep, that it could be misinterpreted as "having lost the mode." That is, in using the Arnoldi algorithm to trace the eigenvalue corresponding to the *type*-I mode downstream in $x_\perp$, the mode of interest could have been lost for a different eigenvalue. This is not what happens in this occassion, which is demonstrated by that the drop is resolved with 7 to 16 $x_\perp$-steps, depending on the z-harmonic. Moreover, the eigenmode computed with the local approach gradually develops a secondary spatial structure that is dominant around the top of the crossflow vortex (shown in Fig. 12(*b*)) from a relatively far upstream location: $x_\perp/\delta_0 \geq 350$. This structure emerges when using a local approach whether one accounts for $\partial\mathring{\overline{Q}}/\partial x$-terms or not. The viscous dissipation attributed to this secondary structure causes the abrupt quenching of the disturbance around $x_\perp/\delta_0 = 400$. This secondary structure, akin to the shape commonly attributed to the *type*-II instability, appears neither in the DNS nor in the plane-marching results. Therefore, this conclusively identifies the disturbance-evolution history, captured by the plane-marching approach, as the physical aspect responsible for preventing the secondary, *type*-II-like structure from emerging alongside the typical *type*-III shape function. The streamwise invariance of the disturbance prescribed by the local approaches enables the disturbance to settle in a position in the local zy-plane, whether it sees the streamwise changes in the distorted base flow or not, while it quickly vacates this position when it is itself allowed to evolve in the streamwise direction.

This situation demonstrates that the plane-marching approach yields a significant qualitative improvement over local results for the *type*-III disturbance at 1 kHz. Moreover, it shows that local results can yield false speculation as to non-linear effects. The same authors of the present article mistook the departure of the local results from the DNS results as being caused by non-linear processes in Ref. [22, first paragraph of page 14]. With the insight gained from the plane-marching approach, this speculation is now determined to be incorrect. Instead, the departure is caused by neglecting the *linear*, disturbance-evolution history. Apparently, the *type*-III disturbance amplitude is small enough for the linear plane-marching approach to accurately approximate the disturbance evolution as observed in the DNS within the presently considered domain.

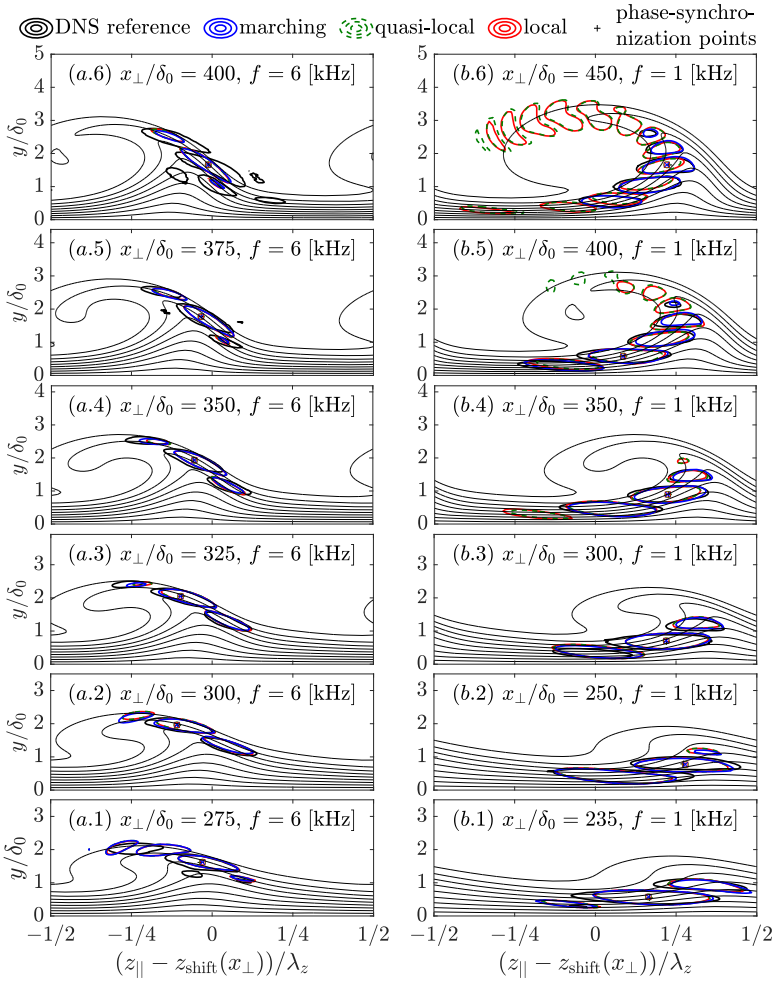

Fig. 12. Isocontours of instantaneous, leading-edge-orthogonal velocity perturbation (level: 30 % of instantaneous, in-plane maximum; phase of stability results: aligned to DNS at in-plane location where maximum is achieved, location indicated by symbols) for *type*-I (*a*) and -III (*b*). Isocontours of distorted base flow velocity in the direction of the inviscid streamline $\overset{\circ}{U}_s$ (10 %, 20 %, …, 90 % of free-stream value).

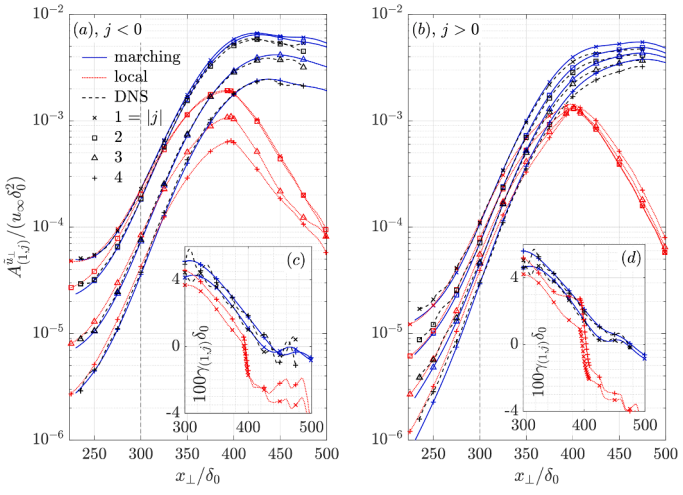

Fig. 13. Perturbation amplitudes (panels *a*,*b*) and growth rates (insets *c*,*d*) for the *z*-Fourier harmonics $|\tilde{u}|_{(1,j)}$ at 1 kHz attributed to the *type*-III instability mechanism. Amplitudes of the linear approaches' $|\tilde{u}|_{(1,-1)}$-harmonics match the DNS equivalent at $x_\perp/\delta_0 = 300$ (vertical dashed line). The steep growth-rate drop is shown to be resolved by plotting a marker for every $x_\perp$-step in panels (*c*,*d*); the same range is highlighted by 3 markers in panels (*a*,*b*).

3.4. Delayed neutral point for type-II instability

As briefly pointed out before, Fig. 8 shows that the neutral point for the *type*-II instability mechanism as computed with the plane-marching approach(es) ($x_\perp/\delta_0 = 320.97 - 321.94$, see Table 3) is located significantly farther downstream than the equivalent result computed with both the quasi-local ($x_\perp/\delta_0 = 292.93$) and local ($x_\perp/\delta_0 = 294.06$) approaches. Although the *type*-I and -III disturbances display a similar behavior (they are respectively shifted downstream by $0.52\lambda_z - 0.62\lambda_z$ and $0.72\lambda_z$), this distance is especially large for *type*-II ($2.77\lambda_z$ to $2.98\lambda_z$). This finding is highly important in relation to the difficulties that the present study and studies presented in the literature [9,10,44] have faced regarding the effective forcing of the *type*-II mechanism in DNS. Although they considered different conditions, our findings about *type*-II could explain the similar observations of Wassermann and Kloker [9, Figs. 21 & 22]. If the forcing function is placed slightly upstream of the neutral point (both $x_{\perp,\text{start}}$ and $x_{\perp,\text{end}} \lesssim x_{\perp,\text{n}}$) as predicted by the quasi-local and local approaches, the introduced disturbance will decay significantly before it reaches the neutral point as predicted by the plane-marching approaches. Hence, if the forcing amplitude is small, no signal can be accurately resolved downstream. If instead the forcing amplitude is large, one triggers other large-amplitude disturbance mechanisms in the immediate vicinity of the forcing function. If the true neutral point lies far enough downstream of the forcing function, then the forcing would necessarily be inefficient and, in the extreme case, an amplitude to effectively trigger the *type*-II mechanism does not exist.

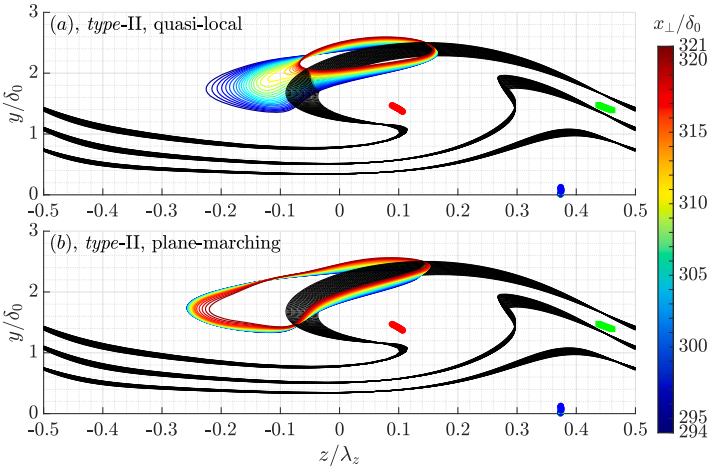

Fig. 14. Isocontours of $|\tilde{u}_\perp|$ (level: 50 % of in-plane maximum) for *type*-II at 8 kHz as computed with the quasi-local (*a*) and plane-marching (*b*, $s = 0$, i.e. no stabilization) approach. Isocontours of distorted base flow velocity $\overline{\overset{\circ}{U}}_\perp$ (50 %, 70 %, and 90 % of free-stream value). Saddle (green square) and centers (red circle: anti-clockwise; blue circle: clockwise rotation) generated by the $\overline{\overset{\circ}{V}}$- and $\overline{\overset{\circ}{W}}$-components: $\overline{\overset{\circ}{V}} = \overline{\overset{\circ}{W}} = 0$.

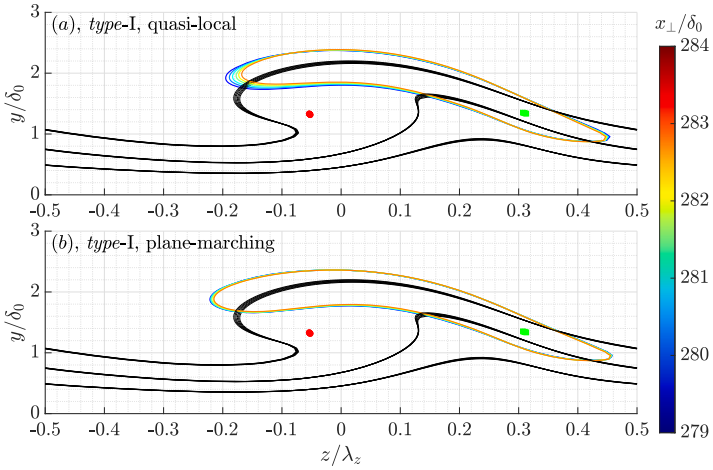

Fig. 15. Isocontours of $|\tilde{u}_\perp|$ (level: 14.29 % (1/7) of in-plane maximum) for *type*-I at 6 kHz as computed with the quasi-local (*a*) and plane-marching (*b*, $s = \delta_0$) approach. Isocontours of distorted base flow velocity $\overline{\overset{\circ}{U}}_\perp$ (50 %, 70 %, and 90 % of free-stream value). Saddle (green square) and centers (red circle: anti-clockwise; blue circle: clockwise rotation) generated by the $\overline{\overset{\circ}{V}}$- and $\overline{\overset{\circ}{W}}$-components: $\overline{\overset{\circ}{V}} = \overline{\overset{\circ}{W}} = 0$.

To investigate why this mechanism is uniquely pronounced for the *type*-II disturbance, we study the solutions' behavior at streamwise $x_\perp$-locations in-between the neutral point as computed with the quasi-local approach ($x_\perp/\delta_0 = 294$) and that with a plane-marching approach ($x_\perp/\delta_0 = 321$). Within the scope of the deductions that are to follow, the local approach produces indistinguishable results to those obtained with the quasi-local approach. Traces of the eigen-/shape functions for the *type*-II mechanism are shown in Fig. 14. The plane-marching approach is initialized with the quasi-local result at $x_\perp/\delta_0 = 290$ in this case. While the shape function computed with the plane-marching approach continues to occupy the region on the left of the crossflow vortex ($z/\lambda_z \in [-0.25, -0.09]$) over this $x_\perp$-range, the quasi-local eigenfunction moves to the crest (i.e., to the top) of the vortex. Interestingly, the neutral instances of the quasi-local (blue isocontour) and plane-marching (red isocontour) solutions have very similar spanwise extents to the left of the crossflow vortex (both reach past $z/\lambda_z = -0.2$).

The apparent motion of the quasi-local eigenfunction to the top of the vortex goes against the flow imposed by the in-plane velocity components $\overline{\overset{\circ}{V}}$ and $\overline{\overset{\circ}{W}}_{||}$, which are respectively directed down- and leftward in the region where the eigenfunction is dominant. Technically, this apparent disturbance motion in the opposite direction of the local advection is possible if the disturbance is subjected to a sufficiently strong dissipation in the region $z/\lambda_z \in [-0.25, -0.09]$. However, the behavior of the plane-marching solution demonstrates that the motion of the quasi-local solution is heavily exaggerated. The plane-marching approach accounts for the disturbance's streamwise evolution history, including the in-plane advection, which counteracts the tendency of the local disturbance eigenfunction to move to the vortex crest. This causes the history-aware shape function to linger in the region $z/\lambda_z \in [-0.25, -0.09]$. The cause of the qualitatively nonphysical behavior of the quasi-local solution is solely attributable to the streamwise evolution history of the disturbance that is not captured by the (quasi-)local approaches. Both the local and quasi-local approach simulate a nonphysical local equilibrium, that is unachievable if the disturbance is aware of its streamwise evolution history.

To illustrate why this effect is present but far less pronounced for the *type*-I disturbances, we also show the behavior of the *type*-I solutions at streamwise $x_\perp$-locations in-between the neutral point as computed with the quasi-local approach ($x_\perp/\delta_0 = 279$) and that with a plane-marching approach ($x_\perp/\delta_0 = 284$); in this case, the plane-marching solution is initialized with the quasi-local result at $x_\perp/\delta_0 = 275$. The trace of the eigen-/shape functions for the *type*-I mechanism are shown in Fig. 15. Again, the quasi-local solution shows a more emphasized rightward motion versus the plane-marching solution, but these motions are much reduced as compared to those of the *type*-II solutions (also note the much smaller isolevel shown for *type*-I than for *type*-II). These effects compound to explain that the *type*-I neutral points are located slightly farther downstream as computed with the plane-marching approach versus the quasi-local approach, but to a much smaller extent than that recorded for the *type*-II neutral points.

This difference between the *type*-I and -II disturbances directly relates to the strong influence of the in-plane flow as addressed by Bonfigli and Kloker [10] and Groot et al. [32]. Whereas *type*-I disturbances are trapped around the saddle formed by the in-plane flow and therefore have a relatively stable in-plane position, the *type*-II disturbances do not overlap such points and hence form a precarious equilibrium between in-plane advection and Reynolds-stress production terms.

The neutral instances of the *type*-III eigen-/shape functions are located very close to the wall and still connect across the spanwise periodic boundaries. Hence, the advection effects induced by the in-plane flow are practically imperceptible.

4. Conclusion

We provided a detailed derivation, analysis, and verification of the non-orthogonal, plane-marching Parabolized Stability Equations (PSE) approach. A formulation in a non-orthogonal coordinate system enables simultaneously spanning the direction in which the crossflow vortex is periodic and the direction in which the base flow, distorted by the primary crossflow instability, evolves slowest. Thereby, the effect of the simplifying assumptions for the plane-marching stability approach regarding spatial evolution are minimized. Two local approaches were also considered: in the (proper/consistent) local approach, we drop all out-of-plane derivatives of the distorted base flow, while we keep those terms in what we call the quasi-local approach.

We demonstrated that the stabilization approach of Andersson et al. [17] enables achieving converged plane-marching solutions for a broad frequency range if residual ellipticity of the system would otherwise cause divergence. Therefore, we do not have to drop the pressure gradient term, that can potentially have an important impact on the solution behavior, even if dropping this term yielded practically identical

results for the particular conditions considered in this article (a broad frequency range, but a specific crossflow vortex).

We performed several verification studies. First, we demonstrate that solutions converge versus grid size in all dimensions; this was specifically performed for the primary traveling crossflow (TCF) disturbance at 300 Hz, the distorted equivalent of the TCF disturbance (*type*-III) at 1 kHz, and the proper secondary *type*-I disturbance at 6 kHz. Second, we matched the aforementioned TCF disturbance against a result computed with a line-marching PSE approach. Third, we matched the amplitude, growth-rate, and disturbance shape evolution against Direct Numerical Simulations (DNS) for the aforementioned *type*-I and -III disturbances.

For *type*-III, the plane-marching approach yields both quantitative and qualitative improvement over both local approaches that emphasizes the merits of the plane-marching approach. At the particular frequency, 1 kHz, and particular crossflow vortex considered, we find that the *type*-III disturbance as modeled by the local approaches develops a secondary structure in its shape function, akin to the shape of the *type*-II instability, that causes the growth rate to steeply drop. This structure neither emerges in the plane-marching results nor DNS. Therefore, we can conclude that the upstream evolution history of the disturbance is responsible for preventing this *type*-II-like structure from occurring.

Lastly, we observed that the plane-marching solutions for *type*-I, -II, and -III disturbances display delayed neutral points as compared to results computed with both local approaches. The delay for the *type*-II instability is especially pronounced and corresponds to approximately 3 crossflow-vortex wavelengths. The results suggest that this is a consequence of the nonphysical movement of the *type*-II shape function against the in-plane velocity field near the neutral point, when modeled with a local approach. This may explain why DNS results for the *type*-II disturbance are scarce in the literature.

CRediT authorship contribution statement

Koen J. Groot: Writing – review & editing, Writing – original draft, Visualization, Validation, Supervision, Software, Resources, Project administration, Methodology, Investigation, Formal analysis, Data curation, Conceptualization; **Jordi Casacuberta:** Writing – review & editing, Visualization, Validation, Software, Resources, Investigation, Formal analysis, Data curation; **Stefan Hickel:** Writing – review & editing, Conceptualization.

Data availability

Data will be made available on request.

Declaration of competing interest

The authors declare that they have no known competing financial interests or personal relationships that could have appeared to influence the work reported in this paper.

Acknowledgement

We sincerely thank Marios Kotsonis at Delft University of Technology for the useful conversations; they greatly contributed to this manuscript's quality. **Funding.** The direct numerical simulations were carried out on the Dutch national e-infrastructure with the support of SURF Cooperative.

References

[1] White EB, Saric WS. Secondary instability of crossflow vortices. J Fluid Mech 2005;525:275–308.
[2] Balachandar S, Streett CL, Malik MR. Secondary instability in rotating-disk flow. J Fluid Mech 1992;242:323–47.
[3] Malik MR, Li F, Chang C-L. Crossflow disturbances in three-dimensional boundary layers: nonlinear development, wave interaction and secondary instability. J Fluid Mech 1994;268:1–36.
[4] Malik MR, Li F, Choudhari MM, Chang C-L. Secondary instability of crossflow vortices and swept-wing boundary-layer transition. J Fluid Mech 1999;399:85–115.
[5] Koch W, Bertolotti FP, Stolte A, Hein S. Nonlinear equilibrium solutions in a three-dimensional boundary layer and their secondary instability. J Fluid Mech 2000;406:131–74.
[6] Zhou Y. Hydrodynamic instabilities and turbulence: Rayleigh–Taylor, Richtmyer–Meshkov, and Kelvin–Helmholtz mixing. Cambridge University Press; 2024.
[7] Zhou Y, Sadler JD, Hurricane OA. Instabilities and mixing in inertial confinement fusion. Annu Rev Fluid Mech 2025;57:197–225.
[8] Zhou Y. Rayleigh–Taylor and Richtmyer–Meshkov instability induced flow, turbulence, and mixing. II. Phys Rep 2017;723:1–160.
[9] Wassermann P, Kloker M. Mechanisms and passive control of crossflow-vortex-induced transition in a three-dimensional boundary layer. J Fluid Mech 2002;456:49–84.
[10] Bonfigli G, Kloker M. Secondary instability of crossflow vortices: validation of the stability theory by direct numerical simulation. J Fluid Mech 2007;583:229–72.
[11] Li F, Choudhari MM. Spatially developing secondary instabilities in compressible swept airfoil boundary layers. Theor Comp Fluid Dyn 2011;25(1):65–84.
[12] Groot KJ, Eppink JL. Stability analysis of the flow over a swept forward-facing step using PIV base flows in a nonorthogonal coordinate system. AIAA Pap 2021–2908 2021.
[13] Paredes P. Advances in global instability computations: from incompressible to hypersonic flow. Universidad Politécnica de Madrid: PhD Dissertation 2014.
[14] Paredes P, Hanifi A, Theofilis V, Henningson DS. The nonlinear PSE-3d concept for transition prediction in flows with a single slowly-varying spatial direction. Procedia IUTAM 2015;14:36–44.
[15] Ambrosino B, Tocci F, Theiß A, Hein S, Rodríguez D. Stationary crossflow vortices' secondary instability: linear stability theory and parabolized stability equations. AIAA J 2025;63.6:2182–98.
[16] Casacuberta J, Hickel S, Westerbeek S, Kotsonis M. Direct numerical simulation of interaction between a stationary crossflow instability and forward-facing steps. J Fluid Mech 2022;943:A46.
[17] Andersson P, Henningson DS, Hanifi A. On a stabilization procedure for the parabolic stability equations. J Eng Math 1998;33:311–32.
[18] Rius-Vidales AF, Kotsonis M. Influence of a forward-facing step surface irregularity on swept wing transition. AIAA J 2020;58(12):5243–53.
[19] Rius-Vidales AF, Kotsonis M. Impact of a forward-facing step on the development of crossflow instability. J Fluid Mech 2021;924:A34.
[20] Rius-Vidales AF, Kotsonis M. Unsteady interaction of crossflow instability with a forward-facing step. J Fluid Mech 2022;939:A19.
[21] Casacuberta J, Hickel S, Kotsonis M. Mechanisms of interaction between stationary crossflow instabilities and forward-facing steps. AIAA Pap 2021-0854 2021.
[22] Casacuberta J, Groot KJ, Hickel S, Kotsonis M. Secondary instabilities in swept-wing boundary layers: direct numerical simulations and BiGlobal stability analysis. AIAA Pap 2022–2330 2022.
[23] Hickel S, Adams NA. Implicit LES applied to zero-pressure-gradient and adverse-pressure-gradient boundary-layer turbulence. Int J Heat Fluid Flow 2008;29:626–39.
[24] Hickel S, Egerer CP, Larsson J. Subgrid-scale modeling for implicit large eddy simulation of compressible flows and shock-turbulence interaction. Phys Fluids 2014;26:106–101.
[25] Casacuberta J, Groot KJ, Ye Q, Hickel S. Transitional flow dynamics behind a micro-ramp. Flow Turbul Combust 2020;104:533–52.
[26] Åkervik E, Brandt L, Henningson DS, Hoepffner J, Marxen O, Schlatter P. Steady solutions of the Navier-Stokes equations by selective frequency damping. Phys Fluids 2006;18(6):068102.
[27] Casacuberta J, Groot KJ, Tol HJ, Hickel S. Effectivity and efficiency of selective frequency damping for the computation of unstable steady-state solutions. J Comput Phys 2018;375:481–97.
[28] Saric WS, Reed HL, White EB. Stability and transition of three-dimensional boundary layers. Annu Rev Fluid Mech 2003;35(1):413–40.
[29] Groot KJ. Derivation of and simulations with BiGlobal stability equations. M.Sc. thesis; Delft University of Technology; The Netherlands; 2013.
[30] Aris R. Vectors, tensors, and the basic equations of fluid mechanics. Dover Publications; 1989. ISBN ISBN: 0-486-66110-5.
[31] Herbert T. Parabolized stability equations. Annu Rev Fluid Mech 1997;29:245–83.
[32] Groot KJ, Serpieri J, Pinna F, Kotsonis M. Secondary crossflow instability through global analysis of measured base flows. J Fluid Mech 2018;846:605–53.
[33] Chakraborty P, Balachandar S, Adrian RJ. On the relationships between local vortex identification schemes. J Fluid Mech 2005;535:189–214.
[34] Groot KJ. BiGlobal stability of shear flows spanwise & streamwise analyses. Ph.D. thesis; TU Delft and von Karman Institute for Fluid Dynamics; 2018.
[35] Li F, Malik MR. Mathematical nature of parabolized stability equations. In: Laminar-turbulent transition: IUTAM symposium, sendai/japan, september 5–9, 1994. Springer; 1995, p. 205–12.
[36] Li F, Malik MR. On the nature of PSE approximation. Theor Comp Fluid Dyn 1996;8(4):253–73.
[37] Haj-Hariri H. Characteristics analysis of the parabolized stability equations. Stud Appl Math 1994;92(1):41–53.
[38] Vigneron Y, Rakich J, Tannehill J. Calculation of supersonic viscous flow over delta wings with sharp subsonic leading edges 1978;:NASA-TM-78500.
[39] Briggs RJ. Electron-stream interaction with plasmas. The MIT Press; 1964.
[40] Huerre P, Monkewitz PA. Absolute and convective instabilities in free shear layers. J Fluid Mech 1985;159:151–68.
[41] Huerre P, Monkewitz PA. Local and global instabilities in spatially developing flows. Annu Rev Fluid Mech 1990;22(1):473–537.

[42] Fedorov A, Tumin A. High-speed boundary-layer instability: old terminology and a new framework. AIAA J 2011;49(8):1647–57.
[43] Tumin AT, Aizatulin L. Instability and receptivity of laminar wall jets. Theo Comput Fluid Dyn 1997;9(1):33–45.
[44] Högberg M, Henningson D. Secondary instability of cross-flow vortices in Falkner–Skan–Cooke boundary layers. J Fluid Mech 1998;368:339–57.